

GRAIN PROPERTIES OF COMET C/1995 O1 (HALE-BOPP)

DAVID E. HARKER^{1,2} AND DIANE H. WOODEN²

NASA Ames Research Center, Space Science Division, MS 245-3, Moffet Field, CA 94035-1000

CHARLES E. WOODWARD²

Department of Astronomy, University of Minnesota, 116 Church Street SE, Minneapolis, MN 55455

AND

CAREY M. LISSE

Department of Astronomy, University of Maryland, College Park, MD 20742

Received 2001 July 2; accepted 2002 July 23

ABSTRACT

We present the analysis of 7.6–13.2 μm infrared (IR) spectrophotometry ($R \approx 250$) of comet C/1995 O1 (Hale-Bopp), in conjunction with concurrent observations that extend the wavelength coverage of the spectral energy distribution from near- to far-infrared wavelengths. The observations include temporal epochs preperihelion (1996 October and 1997 February UT), near perihelion (1997 April UT), and postperihelion (1997 June UT). Through the modeling of the thermal emission from small, amorphous carbon grains and crystalline and amorphous silicate grains in Hale-Bopp's coma, we find that as the comet approached perihelion, the grain size distribution (the Hanner modified power law) steepened (from $N = 3.4$ preperihelion to $N = 3.7$ near and postperihelion), along with an increase in the fractal porosity of larger (greater than 1 μm) grains. The peak of the grain size distribution remained constant ($a_p = 0.2 \mu\text{m}$) at each epoch. We attribute the emergence of the 9.3 μm peak near perihelion to crystalline orthopyroxene grains released during epochs of high jet activity. Crystalline silicates (olivine and orthopyroxene) make up about 30% (by mass) of the sub-micron-sized ($\leq 1 \mu\text{m}$) dust grains in Hale-Bopp's coma during each epoch.

Subject headings: comets: general — comets: individual (C/1995 O1 Hale-Bopp) — infrared: solar system

1. INTRODUCTION

Comets are the least processed remnants from the early solar nebula era of dust grain formation and subsequent agglomeration into planetesimals. These early grain formation processes are important in understanding how dust grains in the solar nebula condensed, collided, and grew into centimeter-sized bodies, the building blocks of protoplanetesimals, out of which grew our solar system. Linking the mineralogy and morphology of the rock-forming elements to the accumulation and growth of protoplanetesimals is complicated by the fact that meteorites (of which we have a large sample) have suffered heating and modification in the accumulation process. Chondrules, a major building block of inner solar system bodies (such as meteorites), have been shown to be melted conglomerates (see, e.g., Morfill, Durisen, & Turner 1998). Comets and the interplanetary dust particles (IDPs) that comets shed in their comae are the principal survivors from the early solar nebula.

IDPs have been shown to contain silicates both amorphous and crystalline in structure (Bradley et al. 1999b). The predominant silicate species are olivine ($[\text{Mg}_y\text{Fe}_{1-y}]_2\text{SiO}_4$, where $0 \leq y \leq 1$) and pyroxene ($[\text{Mg}_x\text{Fe}_{1-x}]\text{SiO}_3$, where $0 \leq x \leq 1$). A value of $x = y = 1$ denotes the Mg-pure end member of the mineral, and a value of $x = y = 0$ denotes the Fe-pure end member. Contained within IDPs are what are known as glasses with embedded metal and sulfides, or GEMS. These GEMS are

thought to be amorphous silicates, accreted into the outer solar nebula from the interstellar medium (ISM; Bradley, Brownlee, & Snow 1997), that are then incorporated into cometary bodies. Mg-rich silicate crystals are also held within IDPs (Bradley, Humecki, & Germani 1992) and are detected through cometary spectra (Hanner et al. 1999; Wooden et al. 1999, 2000a). If these Mg-rich crystals are solar nebula condensates, then they must have formed in an environment close to the Sun (1–5 AU) (Bell et al. 2000). In this 1–5 AU region, the temperature is hot enough (~ 1500 K) that Mg-rich silicate crystals are preferentially condensed (Grossman 1972). On the other hand, the Mg-rich crystals may be Mg-rich amorphous silicates that were annealed at temperatures of ~ 1000 K (Hallenbeck, Nuth, & Daukantus 1998). The Mg-rich crystals represent grains processed at high temperatures in the inner nebula. For incorporation into cometary bodies, these silicate crystals were then mixed out to large radial distances (Bockelée-Morvan et al. 2002) without experiencing reheating events, since reheating leads to the incorporation of Fe back into the silicates (Weisberg, Zolensky, & Prinz 1997; Krot, Scott, & Zolensky 1997). Therefore, Mg-rich crystals in comets probe physical conditions and processes in the early solar nebula.

Our knowledge of comet grains results from a combination of analytical modeling of spectra, the laboratory study of IDPs, and in situ measurements (e.g., comet Halley and the future *Stardust* mission). The constraints on the mineralogy, porosity, and size distribution of comet grains from spectra are consistent with IDPs and in situ measurements. The affirmation of the analysis techniques is also important for the study of amorphous and crystalline silicates in isolated pre-main-sequence systems (e.g., *Infrared Space*

¹ National Research Council Associate.

² Visiting Astronomer at the Infrared Telescope Facility, which is operated by the University of Hawaii under contract with the National Aeronautics and Space Administration.

Observatory Short Wavelength Spectrometer [ISO SWS] observations of Herbig Ae/Be stars; Waelkens, Malfait, & Waters 1999). The study of cometary grains provides a foundation for connecting grain properties to processes in protoplanetary disk environments.

This paper examines the dust grain morphology of Comet C/1995 O1 (Hale-Bopp). Since Hale-Bopp was detected at a large heliocentric distance (~ 7 AU) and showed activity (gas and dust production) greater than any other observed comet at the same heliocentric distance, astronomers were provided a unique opportunity to monitor Hale-Bopp through a large range of distances pre- and postperihelion. An extensive observing campaign was conducted to collect near-infrared (NIR) imaging data and mid-infrared (~ 10 μm) spectrophotometry at a resolution of $R = \lambda/\Delta\lambda \approx 200$ over 0.93–2.8 AU. Using the HIFOGS spectrophotometer, Wooden et al. (1999) performed an empirical mineralogical study of the silicate resonance features of Hale-Bopp, identifying the temperature evolution of the silicate minerals (especially crystalline orthopyroxene) as the comet approached and receded from perihelion. Here, that work is built on by starting with the Wooden et al. (1999) mineralogy. Through grain modeling, we constrain the morphological properties of the dust grains, including size distribution, porosity, and the relative amounts of the materials. The temperature evolution determined from observations at various heliocentric distances is key to constraining the grain properties.

Our observations are presented in § 2; § 3 lists the model parameters for fitting the synthetic spectra to the data, as well as presenting general grain properties derived from the analytical modeling; § 4 presents the model fits to the spectral energy distribution (SED) of Hale-Bopp; § 5 discusses the results of the modeling; and § 6 summarizes the results.

2. OBSERVATIONS

2.1. HIFOGS Spectrophotometry

Spectrophotometry of comet Hale-Bopp was obtained using the NASA Ames Research Center High Efficiency Faint Object Grating Spectrometer (HIFOGS; Witteborn et al. 1991) at the 2.3 m Wyoming Infrared Observatory (WIRO) and the 3 m NASA Infrared Telescope Facility (IRTF). The HIFOGS observations cover four distinct tem-

poral epochs of the 1997 apparition of comet Hale-Bopp, pre- and postperihelion, ranging from a heliocentric distance of 2.8 to 0.93 AU. The HIFOGS spectra discussed here have an approximately constant resolution of $\Delta\lambda \simeq 0.045$ μm per detector over the wavelength interval 7.6–13.3 μm , yielding a resolving power of $R = \lambda/\Delta\lambda \simeq 180$ –350 over the wavelength region. The HIFOGS entrance aperture is 3'' in diameter for all observations. The details of the HIFOGS observations of comet Hale-Bopp are presented in Wooden et al. (1999). Table 1 briefly summarizes the HIFOGS observations used in this work.

The data sets are grouped into four distinct temporal epochs: 1996 October UT (preperihelion), 1997 February UT (preperihelion), 1997 April UT (near perihelion), and 1997 June UT (postperihelion). The spectra in each epoch are scaled to the spectrum with the best spectrophotometry (Wooden et al. 1999). For each set of independent measurements (composed of grating settings separated by $n + 1/2$ detectors to achieve Nyquist sampling), the two (or more) interlaced spectra per epoch agree in shape and flux level with each other within a few percent. Therefore, the differences in the structure of the 10 μm silicate feature measured by HIFOGS for the inner coma (3'') of Hale-Bopp are significant and are used in later analysis (see § 4).

2.2. NIR Imaging

NIR imagery near two of the four temporal epochs spanned by the HIFOGS observations was used to provide a lower limit to the scattered flux from the dust grains (§ 3). Imagery of Hale-Bopp was obtained using the Aerospace Corp. NICMOS3 camera (AEROCAM) at the WIRO on 1996 September 30 UT ($r_h = 2.9$ AU, $\Delta = 2.98$ AU), near the 1996 October 11–14 UT HIFOGS observations. AEROCAM contains a 256×256 pixel HgCdTe array housed in a side-looking dewar that is cooled to liquid nitrogen temperatures (77 K). The spectral region covered by AEROCAM is 0.8–2.5 μm and on WIRO has a plate scale of $0''.43$ pixel $^{-1}$ with a field of view of $110'' \times 110''$. The filter set used for the observations was *J* (1.24 μm), *H* (1.66 μm), and *K*-short (2.15 μm) (Rudy, Rossano, & Puetter 1996). Observations were performed in a staring mode (i.e., no chopping secondary). To correct for the sky signal, sky frames were

TABLE 1
OBSERVATIONAL SUMMARY

UT Date (1)	UT Time (2)	r_h^a (AU) (3)	Δ^b (AU) (4)	Wavelengths (μm) (5)	Scaling Factor (6)
1996 Oct 11	02:06–02:36	2.77	3.02	7.54–12.09	1.00
1996 Oct 12	02:23–02:42	2.76	3.03	7.50–13.12	1.30
1996 Oct 13	01:04–02:22	2.75	3.03	7.50–13.12	1.10
1996 Oct 14	01:16–02:07	2.73	3.03	7.54–12.09	0.95
1997 Feb 14	23:25–23:36	1.28	1.75	7.51–13.07	1.00
1997 Feb 15 ^c	23:57–00:24	1.21	1.73	7.44–12.87	1.04
1997 Apr 11	01:57–02:03	0.93	1.46	7.50–13.98	1.00
1997 Jun 24	20:25–20:53	1.68	2.56	7.53–13.19	1.00
1997 Jun 25	20:12–20:47	1.69	2.57	7.52–13.25	1.08

^a Heliocentric distance of comet Hale-Bopp.

^b Geocentric distance of comet Hale-Bopp.

^c 1997 Feb 15–16 UT.

TABLE 2
COMET HALE-BOPP SED DATA SETS

UT Date (1)	Instrument/ System (2)	$\lambda\lambda$ (in μm) or Photometry Bands (3)	Aperture Diameter (arcsec) (4)	r_h (AU) (5)	Δ (AU) (6)	Scale Factor Derived (7)	Scale Factor SSM ^a (8)	Scaling Method (9)
1996								
Oct 11–14.....	HIFOGS	7.5–13.2	3	2.75	3.03	1.0	1.0	...
Sep 30.....	AEROCAM	<i>JHK</i>	3 ^b	2.90	2.98	1.2	1.0	Scaled with SpectroCam-10
Sep 30.....	SpectroCam-10	7.9–12.5	3 ^b	2.90	2.98	1.2	1.0	7.9 μm boxcar average
Oct 06.....	<i>ISO</i> SWS	6–45	18.9 ^c	2.82	3.01	0.18	0.17	11.2 and 10.0 μm peaks
Oct 07.....	ISOPHOT	3.6–25	23	2.81	3.01	0.14	0.14	10.0 μm boxcar average
1997								
Feb 14–15.....	HIFOGS	7.5–13.2	3	1.21	1.74	1.0	1.0	...
Feb 10.....	URCAM	<i>JHKL M''</i>	3 ^b	1.18	1.0	1.2	1.0	<i>M''</i> to MLOF 4.9 μm
Feb 20.....	MLOF ^d	1.2–18.0	9.3	1.15	1.63	0.25	0.37	7.9 μm boxcar average
Apr 11.....	HIFOGS	7.5–13.2	3	0.93	1.46	1.0	1.0	...
Apr 09.....	OBO ^e	1.2–18.0	27.07	0.93	1.43	0.11	0.17	7.9 μm boxcar average
Jun 24–25.....	HIFOGS	7.5–13.2	3	1.70	2.56	1.0	1.0	...
Jun 10.....	MLOF ^e	1.2–18.0	27.99	1.51	2.04	0.053	0.13	7.9 μm boxcar average

^a SSM = steady-state model.

^b Synthetic aperture.

^c Effective aperture derived from 14×20 rectangular aperture.

^d Photometry from Williams et al. 1997 using Mount Lemmon Observing Facility.

^e Photometry from Mason et al. 2001 using University of Minnesota O'Brien Observatory (OBO) or Mount Lemmon Observing Facility (MLOF).

obtained at a distance from Hale-Bopp of 200'', 400'', and 800'', to ensure that the sky frames were not contaminated by the extended dust tail. The three sky frames were combined by taking the median value of the pixels at each location in the frame to form a single sky frame for each filter.

NIR imagery of Hale-Bopp was also obtained with the University of Rochester Third Generation IR Camera (URCAM; Goetz et al. 1998) at WIRO on 1997 February 10 UT ($r_h = 1.21$ AU, $\Delta = 1.74$ AU). The camera contains a 256×256 InSb array housed in a down-looking dewar cooled with liquid helium to an operating temperature of ≈ 10 K. The wavelength region covered by URCAM is 1–5 μm and on WIRO has a plate scale of $0''.25$ per pixel, or a $64'' \times 64''$ field of view. The broadband filter set used was *J* (1.25 μm), *H* (1.65 μm), *K* (2.23 μm), *L''* (3.81 μm), and *M''* (4.67 μm), which correspond closely to the standard filter set (Elias et al. 1982). Observations were performed in a staring mode, with sky frames taken between source frames. These sky frames were also obtained at a distance of 120'' north of the coma center to avoid contamination from extended emission from Hale-Bopp. The sky frames were median-combined to form a single sky frame for each filter.

Data reduction for all of the images included correction of the pixel-to-pixel variations on the chip by dividing by flat-field frames, subtraction of the sky signal with the sky frames, and flux calibration using values based on observed standard stars to produce flux-calibrated images (Joyce 1992). For AEROCAM, Elias et al. (1982) standard HD 161903 was used for flux calibration, and for URCAM images, Elias et al. (1982) standard HD 162208 was used for flux calibration. Synthetic apertures were applied to the images to obtain photometric data points (see § 2.3). A full analysis of these images will be presented in a future paper (D. Harker et al. in preparation).

2.3. Assembly of Data Sets for SEDs

The assembled SEDs (or λF_λ vs. λ) are composed of data obtained from a total of seven separate data acquisition systems. SEDs include data from the HIFOGS and photometric points derived from our own images (AEROCAM and URCAM). Other data sets used are (1) the *ISO* SWS (6–45 μm) spectrum obtained on 1996 October 6 UT (Crovisier et al. 1997); (2) ISOPHOT (3.6–25 μm) photometry points obtained on 1996 October 7 UT (Grün et al. 2000);³ (3) mid-IR (7.9–12.5 μm) photometric points derived from images obtained on 1996 September 30 UT with the Cornell University SpectroCam-10 imaging spectrograph on the 5 m Hale Telescope at Palomar Observatory (T. L. Hayward 1997, private communication; for details of the observations, see Hayward & Hanner et al. 1997); (4) bolometric photometry points (1.25–18.0 μm) obtained on 1997 February 20 and 1997 June 10 UT at the Mount Lemmon Observing Facility (MLOF) and on 1997 April 09 UT at the University of Minnesota O'Brien Observatory (OBO; for details of the observations, see Williams et al. 1997 and Mason et al. 2001). Details are summarized in Table 2.

At each particular epoch, the relevant data sets are scaled to the corresponding HIFOGS data set for that epoch. The *ISO* SWS spectrum is scaled by matching the 10.0 and 11.2 μm resonance features to the corresponding resonance features measured by the HIFOGS. Photometric data points are derived from the images by using a synthetic aperture of 3'', the size of the HIFOGS entrance aperture. All photometric data sets with a 7.9 μm photometry point are scaled to a photometry point derived by averaging the HIFOGS over the width of the 7.9 μm filter (i.e., “boxcar” average,

³ See <http://www.mpi-hd.mpg.de/galileo/iso/HaleBopp/prelim.html>.

with $\Delta\lambda = 0.5 \mu\text{m}$). The ISOPHOT photometry is scaled to the HIFOGS spectrophotometry at $10 \mu\text{m}$, because the signal-to-noise ratio (S/N) in the ISOPHOT data was highest at $10 \mu\text{m}$. Photometric data points calculated from the URCAM images are scaled by matching the M'' ($4.8 \mu\text{m}$) point to the Williams et al. (1997) $4.9 \mu\text{m}$ data point. The AEROCAM observations are concurrent with the Spectro-Cam-10 observations; therefore, there is no relative scaling correction performed between these two data sets.

A comparison is made between the derived scaling factors and scaling factors calculated assuming a steady-state model (SSM). The SSM for a comet assumes that grains are being ablated off the nucleus at a constant rate and travel through the coma at a constant velocity. This results in a brightness profile for the coma that is inversely proportional to the projected distance from the nucleus (Jewitt 1991). Gehrz & Ney (1992) derived aperture and distance corrections, based on the SSM, that can be applied to temporally different flux observations. Differences between our derived scaling factors and the scaling factors based on the SSM can be the result of (but are not limited to) factors such as (1) aperture geometry (i.e., flux from a square aperture with an effective diameter scaled to a circular aperture); (2) jet activity in the coma producing deviations on short timescale from the SSM assumptions; and (3) jet activity in the coma producing spatial variations in the coma that are measured by the larger apertures and not by the smaller apertures. The largest discrepancy between SSM scaling value and the determined scaling value is for the 1997 June UT epoch. The Mason et al. (2001) values are scaled by a factor 59% greater than that predicted from the SSM.

3. THE GRAIN MODEL

Model spectra are constructed from the emission from dust grains of five distinct and separate mineral species: amorphous olivine, pyroxene, and carbon and crystalline olivine and orthopyroxene. At each epoch, for each material, the grain size distribution has the same functional form, with the amorphous materials ranging in radius $0.1\text{--}100 \mu\text{m}$ and the crystals ranging in radius $0.1\text{--}1 \mu\text{m}$. Crystals are modeled as solid particles at every epoch, while amorphous materials are modeled as fractal, porous dust grains.

The properties of the dust grains in Hale-Bopp's coma are constrained by constructing synthetic spectra using grain-scattering theory and by fitting these synthetic spectra to the assembled spectral and photometric SEDs of comet Hale-Bopp. The methods used are similar to techniques used by previous authors to model dust emission (Reach 1988; Lisse et al. 1998; Hanner et al. 1985; Hanner, Veeder, & Tokunaga 1992, 1996; Krishna Swamy et al. 1988), but use more recent optical constants for putative cometary dust species.

Some authors have successfully modeled the scattering of sunlight in the optical and NIR by using fractal aggregates (Yanamandra-Fisher & Hanner 1999; Petrova 1999). However, sunlight scattered by the dust grains in the coma can be closely approximated by using a simple blackbody (Gehrz & Ney 1992). Using a 5770 K blackbody to represent the light scattered from the dust grains assumes that the grains are comparable in size to the wavelength of light. Since the grains in Hale-Bopp have been found to be small ($a < 0.5 \mu\text{m}$; Williams et al. 1997; Jones & Gehrz 2000), the reflected light in the NIR will be bluer than the solar values.

Therefore, using this approximation will place a lower limit on the flux due to scattered light.

The shape and relative strength of the IR emission from a grain is dependent on the intrinsic properties of the dust (shape, size, and composition), as well as the temperature of the grain. Dust grains are primarily heated through solar radiation and cooled through thermal radiation. Other heating and cooling processes, such as interaction with the solar wind and volatile sublimation, are negligible and are ignored in our radiative equilibrium calculations (Lisse et al. 1998; Lien 1990). To calculate the temperature of the dust grains in the coma, it is assumed that the dust grains are in radiative equilibrium with the solar radiation field. Once the temperature of a grain is determined, the flux produced by a collection of grains of various radii can be easily calculated by assuming a grain size distribution.

The thermal emission from an optically thin collection of grains of a single mineral species at a particular heliocentric distance and wavelength is calculated by integrating over a grain size distribution characterized by a minimum and maximum grain radii a_0 and a_{max} ,

$$F_{\text{em}}(\lambda, r_h) = \frac{N_p}{\Delta^2} \int_{a_0}^{a_{\text{max}}} n(a) \pi a^2 Q_{\text{em}}(a, \lambda) B[\lambda, T_d(a)] da, \quad (1)$$

where N_p is the number of particles at the peak of the grain size distribution if the peak of $n(a)$ is normalized to unity (§ 3.1), Δ is the geocentric distance of the dust grain, $n(a)da$ is the grain size distribution and therefore represents the number of grains between a and $a + da$, $Q_{\text{em}}(a, \lambda)$ is the emission efficiency for a grain of radius a at wavelength λ and is based on the intrinsic properties of the grain (by Kirchoff's Law, Q_{em} is equal to the absorption efficiency of the grain, Q_{abs}), and T_d is the heliocentric distance-dependent (r_h -dependent) dust temperature for a single grain size, a . If it is assumed that there exist multiple mineral species of separate grains within the coma of the comet, the total flux is the sum of the fluxes from the separate mineral species. The resultant model spectrum is compared with the observations of Hale-Bopp, and the particle size distribution and relative contributions of the minerals are adjusted to provide the best χ^2_ν (reduced χ^2) fit to the observed data, where ν is the number of free parameters (Press et al. 1992).

For the analysis of Hale-Bopp, model spectra are computed by integrating over a grain size range of $a_0 = 0.1 \mu\text{m}$ to $a_{\text{max}} = 100 \mu\text{m}$. The lower limit of $0.1 \mu\text{m}$ is chosen because micrometeorite and IDP research reveals that a $0.1 \mu\text{m}$ grain apparently represents the basic structural unit of larger grains and is not easily fragmented to smaller sizes (Hanner 1983; Bradley 1994). Depending on the grain size distribution, $\geq 90\%$ of the thermal flux in the $10 \mu\text{m}$ region arises from grains with radii less than $20 \mu\text{m}$ (Hanner et al. 1985). Therefore, the grain size distribution is truncated at $100 \mu\text{m}$ in radius to avoid excessive computational cycles. Some models were run out to $1000 \mu\text{m}$ within the fitted parameter ranges of the grain size distribution, and the resultant mid-IR flux level and feature shapes were identical to those of models truncated at $100 \mu\text{m}$.

3.1. Grain Size Distribution and Model Grain Properties

Adopting a size distribution of grains in the coma is necessary to calculate the measured flux from the dust. However, the grain size distribution for comets is not well established. Commonly, a power-law distribution,

$n(a)da \propto a^{-\alpha}da$, is adopted. For many comets, Hanner (1983) has shown that a modified power law of the form

$$n(a) = \left(1 - \frac{a_0}{a}\right)^M \left(\frac{a_0}{a}\right)^N \quad (2)$$

provides an adequate model for infrared data ranging from 3.5 to 20 μm . In this equation, a_0 is the minimum grain radius (0.1 μm), N is the slope of the distribution at large a , and M is related to the radius of the peak of the size distribution (i.e., the grain radius at which the grain size distribution rolls over) by

$$a_p = a_0 \frac{(M + N)}{N}. \quad (3)$$

Typically, $3.7 < N < 4.2$ for comets (see Hanner 1984). Model spectra presented in this paper are calculated by adjusting N and M in the Hanner size distribution to provide the best fits. For use in equation (1), $n(a)$ is normalized by the value at the peak of the size distribution, or $n(a_p)$.

Divine & Newburn (1987) propose a grain size distribution based on equation (2), but one in which the peak (a_p) and the width (M) of the distribution can be varied separately. To limit the parameter space for the model SED fits, and for direct comparison with other works (Hayward, Hanner, & Sekanina 2000, hereafter HHS; Li & Greenberg 1997), we do not use the Divine & Newburn grain size distribution in this work. In addition, Harker (1999) finds that using the Hanner size distribution provides better overall fits to the HIFOGS data, compared with fits derived using a straight power law or a Halley-type grain size distribution ($\alpha = -2.0$ for $a < 0.62 \mu\text{m}$; $\alpha = -2.75$ for $0.62 \mu\text{m} < a < 6.2 \mu\text{m}$; $\alpha = -3.4$ for $a > 6.2 \mu\text{m}$; Krishna Swamy et al. 1988). However, note that other authors (Lisse et al. 1998) do not find the Hanner grain size distribution to be adequate for modeling the emission from other comets, such as C/Austin 1990 V, C/Levy 1990 XX, and C/Okazaki-Levy-Rudenko 1989 XX.

As stated in § 3, the intrinsic properties of a dust grain are contained within the optical efficiency of the grain, Q_{em} . Variations in grain properties such as size, shape, and composition (including mineralogy and porosity) are contained within the optical efficiencies. Mie theory (Bohren & Huffman 1983; van de Hulst 1957) is the most common technique used throughout the literature (Lisse et al. 1998; Hanner et al. 1996; Hanner, Lynch, & Russell 1994) to compute the optical efficiencies for grains of given radii, a , and wavelength-dependent indices of refraction, n and k . Mie theory provides the needed flexibility for computing emission and absorption efficiencies for radiative equilibrium and flux spectrum computations. However, Mie theory has limitations, since it calculates the emission from perfectly spherical particles. In particular, Yanamandra-Fisher & Hanner (1999; also § 3.2.3) demonstrate that Mie spheres do not adequately reproduce the correct wavelengths of resonances from silicate crystals.

Dust grains in meteorites and IDPs often are inhomogeneous in shape and composition and highly porous (Bradley 1988). Therefore, fractal, porous dust grains composed of vacuum inclusions in a carbonaceous or siliceous matrix are modeled. Vacuum (for which $n = 1.0$ and $k = 0.0$) is mixed into the dust grains to create a grain density that varies with

size,

$$\rho(a) = \rho_0(a/0.1 \mu\text{m})^{D-3}, \quad (4)$$

where the grain radius, a , is greater than 0.1 μm , ρ_0 is the density of the bulk material, and D is the fractal dimension of the dust. Solid spheres are represented by $D = 3$, while for porous spheres $D < 3$. The fractional filled volume (percent porosity) of the grain is then

$$f = 1 - (a/a_0)^{D-3}, \quad (5)$$

where $a_0 = 0.1 \mu\text{m}$.

To produce these fractal porous dust grains, an effective medium theory (EMT) is employed. EMTs generally used in the literature are Maxwell-Garnett (1904) and Bruggeman (1935). Both theories have been found to provide similar results (Lisse et al. 1998; Chýlek & Videen 1998; Wolff et al. 1994; Bohren & Huffman 1983). However, for an EMT to provide adequate modeling of porous grains, the vacuum inclusions must be Rayleigh-type inclusions spread uniformly throughout the grain matrix (Chýlek & Videen 1998; Krishna Swamy 1997; Wolff et al. 1994; Bohren & Huffman 1983). Bruggeman theory best satisfies these conditions by not distinguishing between the two media being mixed and therefore producing a randomly inhomogeneous medium (Wolff et al. 1994; Bohren & Huffman 1983). This contrasts with Maxwell-Garnett theory, which distinguishes between grain matrix and inclusion. For example, Kozasa, Blum, & Mukai (1992) examine the optical properties of aggregate grains and find that Maxwell-Garnett is a reasonable choice for aggregates that have uniform structures, but is not applicable for those aggregates that have nonhomogeneous structures.

Since spherical particles are implicitly assumed when using Mie theory, Mie theory will not adequately model the emission from particles in which porosity has produced a significant deviation from sphericity. Bazell & Dwek (1990) showed that EMT (either Bruggeman or Maxwell-Garnett) failed to adequately model fractal, porous grains for a fractal dimension of $D < 2$. Therefore, as in Lisse et al. (1998), we take the conservative approach of using a small deviation from a solid sphere, or $2.5 \leq D \leq 3.0$. The values $D = 3.0, 2.857, 2.727, 2.609$, and 2.5 were chosen in the modeling to correspond with values used by Lisse et al. (1998).

The parameters adjusted for the construction of synthetic spectra for comparison with the HIFOGS spectra and aperture photometry are N (slope in the Hanner grain size distribution), M (which determines the peak grain size in the Hanner grain size distribution), D (which determines the degree of fractal porosity in the grains), and N_p (the number of grains at the peak of the grain size distribution [i.e., scaling factor] for each material). As stated above, for a particular epoch, the values of N , M , and D are the same for each material (excluding the crystalline silicates, which always have a value of $D = 3.0$ [solid particles]; § 3.2.3). By adjusting these parameters, the χ^2_{ν} (reduced χ^2) of the fit is minimized to provide the best fit to the data. To aid in performing the calculations (dictated by limiting the number of CPU cycles), the parameters N , M , and D were binned. The slope of the grain size distribution, N , was adjusted ± 0.1 . The peak of the grain size distribution, a_p , as determined by N and M , was also adjusted by a value of

$\pm 0.1 \mu\text{m}$. Therefore, to achieve the range in a_p , M was adjusted by a factor of $\pm N$.

The shape of the model SED is very dependent on variations in the slope of the size distribution (N), the fractal dimension (D), and the peak of the grain size distribution (a_p , and therefore M). Since the model is initially fitted to a flux point at $7.8 \mu\text{m}$, adjustments in N , D , and a_p will affect the model fit most significantly in the $3\text{--}5 \mu\text{m}$ region, as well as longward of $12.5 \mu\text{m}$. While there is a degree of degeneracy between these three parameters, they are tightly constrained with respect to one another. For example, steepening the slope of the grain size distribution (increasing N) will raise the flux in the $3\text{--}5 \mu\text{m}$ region. This rise in flux can be corrected by decreasing the fractal dimension, D (i.e., grains of greater fractal porosity). However, this decrease in D will decrease the flux in the region longward of $12.5 \mu\text{m}$, thereby providing a poorer fit to the data.

At all epochs except 1997 April UT, the 1σ uncertainties in the model parameters are given by those parameter values that produce fits with $\chi^2 = \chi_{\text{min}}^2 + \Delta\chi^2$ (Press et al. 1992), using the theoretical value for $\Delta\chi^2$ ($= 8.18$) for the number of parameters $p = 7$, the number of data points N_{pts} , and the number of free parameters $\nu = N_{\text{pts}} - p$. Since the 1997 April UT HIFOGS data have small 3σ uncertainties, the theoretical value of $\Delta\chi^2$ resulted in an unrealistically small range of parameters; instead, the point of divergence of a multidimensional χ^2 ellipsoid from “flat-bottomed” to “steep-sided” was empirically used (§ 4.3) to define the range of acceptable parameters.

Confidence in the quantitative results inferred from the models is aided by model-independent factors, such as (1) the highly accurate photometric capabilities of the HIFOGS, required to identify subtle changes in the spectral shape of the cometary spectra, including the flux level and slope outside of the $10 \mu\text{m}$ silicate feature; (2) the moderate spectral resolution of the HIFOGS ($R \simeq 180\text{--}360$), sufficient to clearly identify the crystalline silicate resonance features in the spectra; and (3) similar findings from other authors on the grain properties in Hale-Bopp (§ 5.5; HHS; Mason et al. 2001).

3.2. Dust Composition

The mineral assemblages are probable components of cometary dust, as exemplified by chondritic porous interplanetary dust particles (CPIDPs; Bradley et al. 1996). Modeling grain aggregates of various mineralogical compositions, however, is beyond the scope of this work. For this analysis, grains of separate mineral stoichiometries and crystallographic phases are utilized to compute the thermal emission spectra and determine the relative abundances of minerals in comet Hale-Bopp’s coma. By definition of their stoichiometry, minerals are crystalline in form. By observation, materials of the same stoichiometry as the crystalline minerals, but in a disordered (i.e., amorphous) form, have much broader resonances, characteristic of absorption features in the ISM (Li & Greenberg 1997; Demyk et al. 1999). Both amorphous and crystalline forms of minerals are common in IDPs (Bradley et al. 1999c) and Antarctic micrometeorites (AMMs; Bradley et al. 1999b) and are also observed in dust-forming asymptotic giant branch (AGB) stars (Waters et al. 1999; Tielens et al. 1997), pre-main-sequence Herbig Ae/Be stars (Waters & Waelkens 1998),

and comets (Bregman et al. 1987; Krishna Swamy et al. 1988; Hanner et al. 1996; Lisse et al. 1998). In the following discussion, the amorphous form of materials are referred to as amorphous minerals and the crystalline form of materials as crystalline minerals. Furthermore, mineralogy denotes both the mineralogical composition and form (crystalline or amorphous) of the material composing the grain.

3.2.1. Amorphous Silicate Grains

Indices of refraction of amorphous silicate minerals (olivine and pyroxene) published by Dorschner et al. (1995) are used in the modeling because of the completeness of their wavelength coverage. In addition, Dorschner’s laboratory methodologies are aimed at synthesizing interstellar materials. Both amorphous olivine and amorphous pyroxene produce broad resonance features in the 10 and $20 \mu\text{m}$ spectral regions. Specifically, amorphous olivine produces resonances that peak at 9.8 and $17 \mu\text{m}$, and amorphous pyroxene peaks at 9.3 and $18 \mu\text{m}$. The combination of the strong, broad, amorphous silicate resonances contributes to the width of the “ $10 \mu\text{m}$ silicate feature,” extending from as short as $8.2 \mu\text{m}$ to as long as $12.5 \mu\text{m}$. The short-wavelength rise of the silicate resonant feature ($8.2\text{--}10 \mu\text{m}$) can be attributed to the emission from amorphous pyroxene grains (Hanner et al. 1994), while the long-wavelength decline ($11.2\text{--}12.5 \mu\text{m}$) can be attributed to the emission from amorphous olivine grains. Neither olivine nor pyroxene contributes significantly to the emission ($\lesssim 1\%$ of the total emission) at wavelengths shorter than the $10 \mu\text{m}$ silicate feature ($\lesssim 8.2 \mu\text{m}$). However, amorphous silicates can contribute as much as 10% of the total emission at wavelengths longward of the $10 \mu\text{m}$ silicate feature ($\gtrsim 12.5 \mu\text{m}$).

A higher Mg content corresponds to a lower refractive index k (lower attenuation) in the ultraviolet, visible, and NIR (UVIS/NIR). The more Fe in the mineral, the stronger the absorptivity in the UVIS/NIR (Dorschner et al. 1995). Therefore, grains with less Fe and more Mg will be poor absorbers of solar radiation and cooler than their Fe-containing counterparts. Figure 1 illustrates the behavior of amorphous pyroxene grains with various Mg content by plotting temperature versus Mg content for four grain radii at each epoch in which Hale-Bopp was observed. In addition, larger grains are cooler than smaller grains (Fig. 2). Small grains are “superheated” (Gehrz & Ney 1992), compared to perfectly absorbing conducting spheres of the same radius and at the equivalent heliocentric distance. A Mg value of $x = y = 0.5$ for the amorphous olivines and pyroxenes provides the best fit to the data set, based on the spectral shape of the $10 \mu\text{m}$ emission feature (Harker 1999; Fig. 3). This roughly equal abundance of Mg and Fe in the amorphous silicates in Hale-Bopp matches the overall Mg/Fe ratio of anhydrous particles that are composed of many submicron subunits of different composition, including IDPs (Bradley 1988) and comet Halley cluster particles (Schulze, Kissel, & Jessberger 1997).

Figure 4 shows the effect of increasing the fractal dimension D on the absorption efficiency of a $10 \mu\text{m}$ radius amorphous pyroxene grain. At low fractal dimensions, i.e., at high porosity, $10 \mu\text{m}$ -sized grains become less absorbent at short wavelengths and begin to show an emission feature in the 10 and $20 \mu\text{m}$ regions.

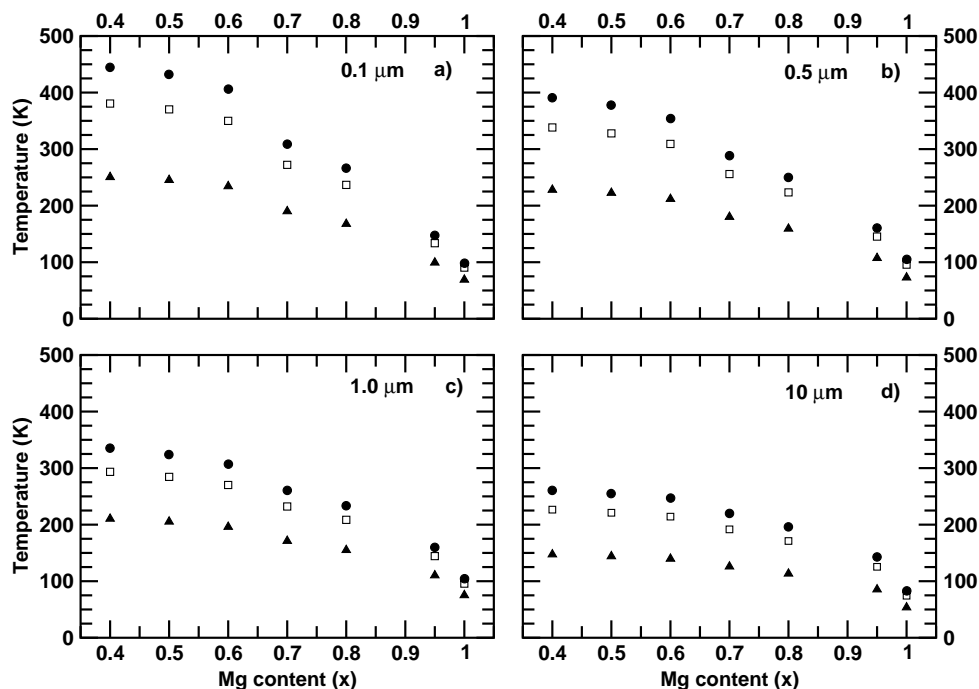


FIG. 1.—Temperature of solid amorphous pyroxene grains ($\text{Mg}_x\text{Fe}_{1-x}\text{SiO}_3$) of varying Mg content (x), for grain sizes $a = 0.1, 0.5, 5.0,$ and $10.0 \mu\text{m}$ ($a-d$, respectively). Heliocentric distances plotted are $r_h = 0.93$ (circles), 1.21 (squares), and 2.80 (triangles) AU.

3.2.2. Amorphous Carbon Grains

A disordered form of carbon, sometimes denoted “glassy carbon,” has been shown to produce continuum emission similar to that observed in comets (Hanner et al. 1985, 1992, 1996). Glassy carbon (optical constants are from Edoh 1983, as suggested for use by Hanner 1988) is used to represent the warm, featureless, absorbing grains that produce the continuum underlying the strong silicate resonances in Hale-Bopp’s SED. At wavelengths shorter than the $10 \mu\text{m}$ silicate feature, most of the underlying thermal emission

($\lesssim 8.2 \mu\text{m}$) is from these warm carbon grains. Although graphite was commonly used to model emission in the ISM, the indices of refraction of graphitic carbon are highly anisotropic (orientation-dependent) and temperature-dependent (Draine & Lee 1984). Furthermore, graphitic carbon is rarely seen in IDPs (Brownlee et al. 2000). Therefore, graphite is not used in modeling the dust emission from Hale-Bopp. The amorphous carbon grains are hotter than Mg-rich silicate grains and therefore have a temperature similar to that of silicate grains with a small Mg/Fe ratio.

The behavior of amorphous carbon grains in the solar radiation field is similar to that of the amorphous silicate grains. At equivalent heliocentric distances, the smaller grains are hotter than larger grains, and the porous grains are cooler than solid grains of equivalent radius, because their vacuous inclusions make them less absorbent at UVIS wavelengths.

3.2.3. Crystalline Silicate Grains

To model the mid- and far-IR emission from crystalline silicate grains, the indices of refraction for olivine from Steyer (1974) and for orthopyroxene from Jäger et al. (1998) were used. However, one problem with these indices is that they do not extend shortward of $3 \mu\text{m}$ (for olivine) and $2 \mu\text{m}$ (for orthopyroxene). That is, they do not cover the entire wavelength range over which we need to perform radiative equilibrium calculations ($0.2-100 \mu\text{m}$). C. Jäger (1998, private communication) performed a preliminary analysis on crystalline materials in the UVIS region and found little difference between the values of the indices of refraction for amorphous and crystalline minerals. Therefore, for Mg-rich orthopyroxene crystals we use the indices of refraction of Mg-rich amorphous pyroxene ($x = 0.95$) for the $0.2-2 \mu\text{m}$ wavelength range. For the same wavelength range, for Mg-rich olivine crystals, the only available indices of refraction

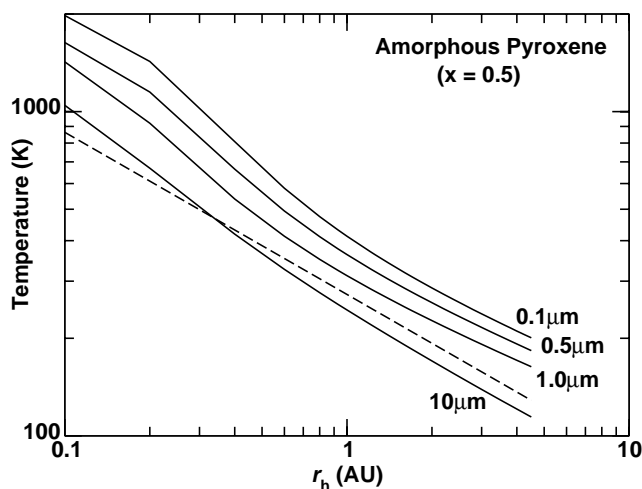


FIG. 2.—Temperature of solid amorphous pyroxene grains ($\text{Mg}_x\text{Fe}_{1-x}\text{SiO}_3$, with $x = 0.5$) due to insolation at different heliocentric distances, for grain sizes $a = 0.1, 0.5, 5.0,$ and $10.0 \mu\text{m}$, as labeled. The dashed line shows the temperature dependence for a perfectly conducting black sphere [$T_{\text{BB}} = 278/(r_h)^{1/2}$].

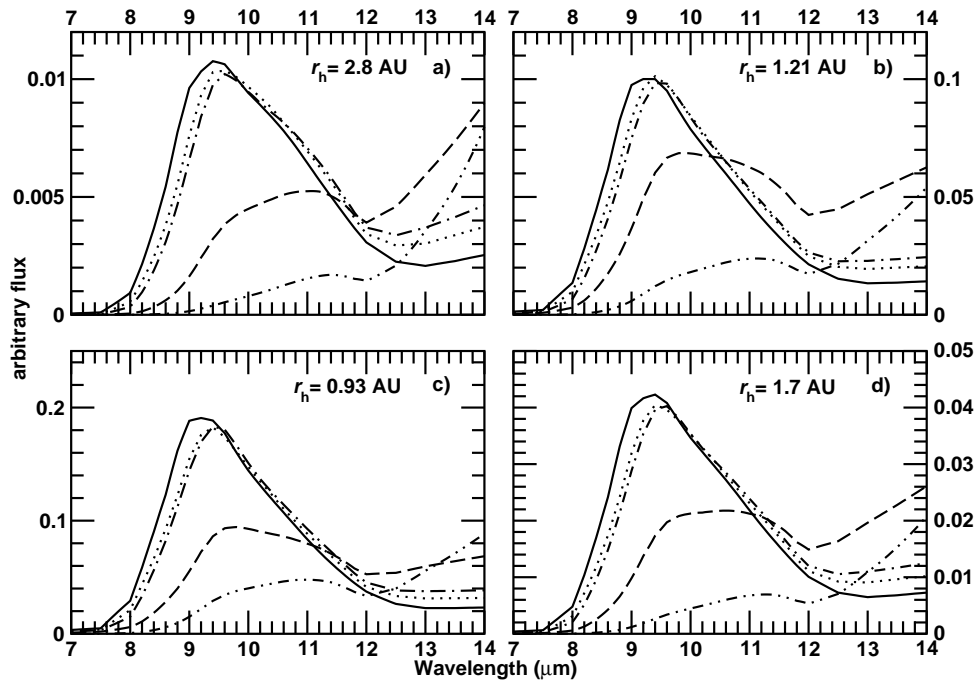


FIG. 3.—Model flux spectra of amorphous pyroxene, computed with Mie theory and using the Hanner size distribution [$n(a) = (1 - a/a_0)^M (a/a_0)^N$], with $N = 3.7$ and $M = 3.7$ ($a_p = 0.2 \mu\text{m}$). Heliocentric distances are 2.8, 1.21, 0.93, and 1.7 AU (a–d, respectively). Plotted are Mg content values (x) of 0.5 (solid line), 0.7 (dotted line), 0.8 (dash-dotted line), 0.95 (long-dashed line), and 1.0 (dash-double-dotted line). Mg content values of 0.4 and 0.6 yield results similar to the $x = 0.5$ line and therefore are not plotted. Note that each epoch is plotted on a separate flux scale.

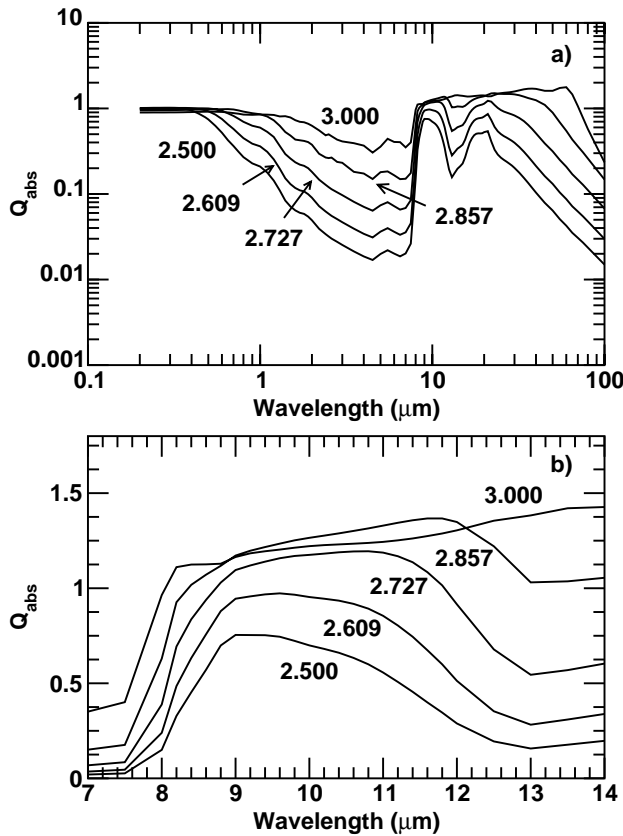


FIG. 4.—Absorption efficiency of an $a = 10 \mu\text{m}$ amorphous pyroxene grain ($x = 0.5$) for (a) the full wavelength range of the indices and (b) the $10 \mu\text{m}$ region in detail. Plotted are fractal porosity values [$f = 1 - (a/a_0)^{D-3}$] for $D = 3.0, 2.875, 2.727, 2.609,$ and 2.5 , which correspond to fractional volume percentages of $f = 0\%, 48.2\%, 71.6\%, 83.5\%,$ and 90.0% .

available are for Mg-poor amorphous olivine ($y = 0.5$). Indices of refraction for Mg-rich ($y = 0.95$) amorphous olivine are extrapolated from the Mg-poor ($y = 0.5$) amorphous olivine indices, using the scaling factors derived from the ratio of Mg-rich ($x = 0.95$) to Mg-poor ($x = 0.5$) amorphous pyroxene. This is the best approach available, since at low Mg contents from 0.2 – $2 \mu\text{m}$, the values of indices of refraction decrease with increasing Mg content at the same rate for amorphous olivine and amorphous pyroxene: the ratios of the indices of refraction of amorphous olivine at $y = 0.5$ – 0.4 equal those of amorphous pyroxene at $x = 0.5$ – 0.4 (Dorschner et al. 1995). Furthermore, at high Mg contents from 0.4 to $2.5 \mu\text{m}$, the values of the indices of refraction also decrease with increasing Mg content at the same rate for crystalline olivine and crystalline orthopyroxene: the ratios of indices of refraction for crystalline olivine at $y = 1.0$ – 0.9 equal those for crystalline orthopyroxene at $x = 1.0$ – 0.9 (Lucey 1998).

The emission from crystalline silicates is difficult to model using Mie theory (Yanamandra-Fisher & Hanner 1999). Therefore, the properties of crystalline grains are constrained by looking to CPIDPs of probable cometary origin. Crystals in CPIDPs are Mg-rich ($x \geq 0.9$), solid, and submicron in size (Bradley et al. 1999b). Adopting these constraints simplifies the modeling of crystalline grains, since Mie theory produces unphysical resonances (i.e., resonances at wavelengths not seen in laboratory transmission measurements) for crystals that are larger than a micron and for porous crystals of any size. Figure 5 shows these unphysical resonances by displaying the absorption efficiency computed for a crystalline olivine grain of radius $5 \mu\text{m}$, a grain of radius $1 \mu\text{m}$ with 10% vacuum, and for comparison, the laboratory-measured absorption spectrum from Koike, Shibai, & Tuchiya (1993).

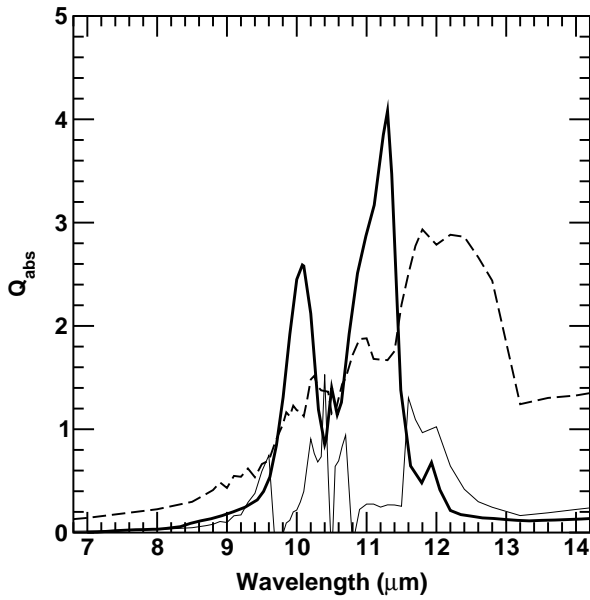


FIG. 5.—Absorption efficiencies of crystalline olivine. The dashed line shows the absorption efficiency for a grain of radius 5 μm computed with Mie theory using the optical constants from Steyer et al. (1974). The three crystallographic axes were averaged together equally. The thin solid line shows the absorption efficiency of a grain of radius 1 μm composed of 10% vacuum. The vacuum was added using the EMT of Bruggeman (1935) and the absorption efficiency computed using Mie theory. For comparison, the thick solid line represents the laboratory-measured absorption of $\sim 0.2 \mu\text{m}$ -sized grains.

Different methods are applied for calculating (1) the temperature of the crystals and (2) the emission from the crystals. Separate methods are needed, since Mie theory does not calculate the correct wavelength position of the crystalline resonances (Yanamandra-Fisher & Hanner 1999). However, Mie theory adequately calculates the height and contrast of the resonance feature with respect to the continuum, compared with laboratory transmission measurements. Therefore, to calculate the temperatures, Mie theory was used to compute the absorption (and emission) efficiencies of solid, submicron-sized grains.

To calculate the emission from the solid, submicron crystals, we use laboratory measurements from Koike et al.

(1993) of the optical extinction (normalized by grain radius, Q_{ext}/a) of Mg-rich crystalline olivine and orthopyroxene powders ($y = 0.9$ and $x = 0.95$, respectively). Values of Q_{ext} are scaled by multiplying by grain radius (between 0.1 and 1 μm). The scaled Q_{ext} -values are used in place of the Q_{abs} -values calculated from Mie scattering in equation (1) to produce model flux spectra. Using the scaled Koike optical efficiencies is adequate for modeling the emission from crystalline olivines and crystalline orthopyroxene, since (1) the grain sizes used in the measurement of Q_{ext}/a by Koike et al. (1993) are 0.2–0.22 μm ; (2) $a \ll \lambda$ in the mid-IR, and therefore the amount of light scattered is negligible, and the amount of light extinguished is approximately equal to the amount of light absorbed, or $Q_{\text{ext}} \approx Q_{\text{em}}$ (see Wooden et al. 1999); (3) based on the emission from amorphous silicates, the 10 μm resonance feature shapes do not change for grain sizes $\leq 1 \mu\text{m}$ (Harker 1999); therefore, we scale the Koike et al. (1993) measurements (by multiplying by grain size) to represent grain sizes between 0.1 and 1 μm ; and (4) the laboratory-measured Q_{ext} for crystalline olivine grains with $a \simeq 0.2 \mu\text{m}$ from Koike match the values and relative peak heights of the Mie theory-calculated Q_{em} from Steyer (1974), excluding the wavelengths of the resonance peaks. Thus, for the olivine and orthopyroxene crystals, we compute the thermal equilibrium temperatures using Mie theory and calculate the emission spectra using the grain size-scaled, laboratory-measured Q_{ext} .

4. MODELING THE EXTENDED SED

Extension of the SED of comet Hale-Bopp beyond the 7.5–13.5 μm spectral coverage of the HIFOGS is possible using photometric data from our own imaging, as well as data obtained by other observers on or near the dates of our observations. Any synthetic spectral model of comet Hale-Bopp must adequately reproduce such SEDs (§ 2.3). The key conclusions resulting from the modeling are (1) the relative abundance of the orthopyroxene crystals increased close to perihelion ($r_h = 0.93 \text{ AU}$); and (2) Hale-Bopp’s grain size distribution steepened (N increased) and the fractal porosity increased (D decreased) during its passage close to the Sun. Table 3 lists the best-fit model parameters and their associated 1 σ correlated errors. The reduced χ^2 ($\chi^2_\nu = \chi^2/\nu$) fit for each epoch is discussed in detail in each of the following sections. Since the bulk of the coma emis-

TABLE 3
MODEL PARAMETERS

UT DATE (1)	r_h (AU) (2)	EPOCH (3)	N^a (4)	M^b (5)	D^c (6)	N_p^d					ν^e (12)	χ^2_ν (13)
						Amorphous Pyroxene ($\times 10^{23}$) (7)	Amorphous Olivine ($\times 10^{23}$) (8)	Amorphous Carbon ($\times 10^{23}$) (9)	Crystalline Olivine ($\times 10^{23}$) (10)	Crystalline Pyroxene ($\times 10^{23}$) (11)		
1996 Oct 11–14.....	2.8	Preperihelion	3.4	3.4	2.8	0.14 ± 0.03	0.15 ± 0.02	0.12 ± 0.02	0.15 ± 0.01	0.03 ± 0.01	542	1.70
1997 Feb 14–15	1.21	Preperihelion	3.7	3.7	2.5	2.48 ± 0.10	1.25 ± 0.06	1.23 ± 0.10	1.55 ± 0.05	0.27 ± 0.05	197	16.36
1997 Apr 11.....	0.97	Near perihelion	3.7	3.7	2.5	2.73 ± 0.22	1.78 ± 0.17	2.22 ± 0.10	3.17 ± 0.10	0.86 ± 0.13	125	99.75
1997 Jun 24–25.....	1.7	Postperihelion	3.7	3.7	2.7	1.23 ± 0.07	0.51 ± 0.05	0.78 ± 0.05	0.95 ± 0.03	0.30 ± 0.02	186	7.48

^a Hanner size distribution: $n(a) = (1 - a_0/a)^M (a_0/a)^N$; $a_0 = 0.1 \mu\text{m}$.
^b Peak grain size: $a_p = a_0(N + M)/N = 0.2 \mu\text{m}$ for every epoch.
^c Fractional filled volume of amorphous grains: $f = 1 - (a/a_0)^{D-3}$.
^d Number of peak grain size grains (i.e., scaling factor).
^e Number of free parameters.

TABLE 4
MASS RATIO TO TOTAL OF SUBMICRON-SIZED GRAINS

UT Dates (1)	Amorphous Pyroxene (2)	Amorphous Olivine (3)	Amorphous Carbon (4)	Crystalline Olivine (5)	Orthopyroxene (6)	Silicate/ Carbon (7)	Crystalline Silicate/ Amorphous Silicate (8)
1996 Oct 11–14.....	0.24	0.25	0.21	0.25	0.05	3.8	0.6
1997 Feb 14–15	0.37	0.18	0.18	0.23	0.04	4.5	0.5
1997 Apr 11.....	0.25	0.17	0.20	0.30	0.08	3.9	0.9
1997 Jun 24–25.....	0.33	0.14	0.21	0.25	0.08	3.8	0.7

sion is from grains with radii $\leq 1 \mu\text{m}$, Table 4 lists the mass fraction of submicron grains for each mineral. The total mass of submicron-sized grains for each mineral was determined by summing over the grain size distribution from 0.1 to $1.0 \mu\text{m}$, to calculate the total number of submicron-sized grains, and then calculating the mass of the total number of grains by assuming a bulk density for the carbon grains of $\rho_c = 2.5 \text{ g cm}^{-3}$ (Lisse et al. 1998) and a bulk density for the silicates of $\rho_s = 3.3 \text{ g cm}^{-3}$ (Dwek 1985).

4.1. 1996 October UT

The synthetic model SED for this epoch (preperihelion) encompasses the $10 \mu\text{m}$ HIFOGS spectra and is extended to include both NIR photometry points and mid- and far-IR *ISO* SWS spectra. The synthetic model SED is constructed by co-adding a blackbody at 5770 K (reflected solar spectrum) and the thermal model flux spectrum, which uses

emission from slightly fractal, porous, amorphous grains ($D = 2.8$) and “hot,” solid, submicron-sized crystalline grains. Figure 6 shows the SED of Hale-Bopp at the 1996 October UT epoch, compared with the best-fit ($\chi^2_r = 1.70$) model SED, using a grain size distribution, with a slope of $N = 3.4$, that peaks at $a_p = 0.2 \mu\text{m}$ ($M = 3.4$). To match the contrast of the resonance peaks with the underlying continuum in both the mid-IR HIFOGS and far-IR *ISO* SWS spectra, the olivine crystals incorporated in the model were calculated to be 1.9 ± 0.1 times hotter than predicted from the pure Mg ($x = 1$) amorphous olivine optical constants (§ 3.2.3). This increase in temperature corresponds to an increase of the Q_{abs} for crystalline olivine in the UVIS by a factor of 74 compared to our Q_{abs} extrapolated to high Mg from Dorschner et al. (1995). The optical constants of Lucey (1998) are an order of magnitude lower than those of Dorschner et al. (1995) and yield a much greater discrepancy between the deduced and calculated temperatures. The

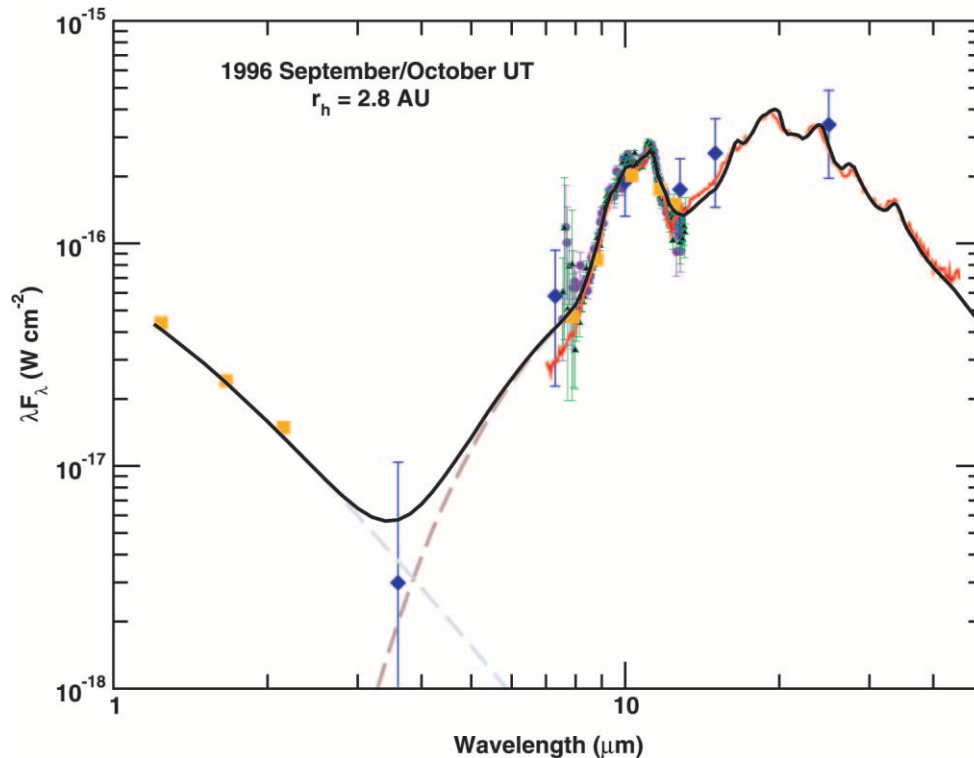


FIG. 6.—Model SED of Hale-Bopp, compared with the observed SED for 1996 October UT. The SED is constructed from data points from HIFOGS spectrophotometry (1996 October 11 and 13 UT, violet circles; 1996 October 12 and 14 UT, green triangles), *ISO* SWS (1996 October 6 UT, red line), synthetic-aperture photometry from AEROCAM and SpectroCam-10 imaging (1996 September 30 UT, orange squares), and ISOPHOT (1996 October 7 UT, blue diamonds). A synthetic spectral model fit (black line) is constructed from a 5770 K blackbody (dashed gray line) and the calculated thermal model (dashed brown line). This synthetic model is fitted to the SED with $\chi^2_r = 1.70$ and best-fit parameters $N = 3.4$, $M = 3.4$ ($a_p = 0.2 \mu\text{m}$), and $D = 2.875$. The abundances by number at the peak of the grain size distribution are listed in Table 3.

empirically determined temperature of crystalline olivine is currently the best method to determine the flux spectrum for crystalline olivine until a homogeneous set of optical constants is available over the entire wavelength range ($\lambda = 0.1\text{--}50\ \mu\text{m}$).

At 2.8 AU, the “hot” olivines range in temperature between 155 and 168 K (between grain sizes 0.1 and 1.0 μm). The temperature of a blackbody grain at this heliocentric distance is 166 K. Therefore, the assignment of the blackbody temperature to the crystalline olivines is a good first-order approximation, as is done by other investigators (HHS; Wooden et al. 1999). For consistency, the crystalline orthopyroxene grains are heated by the same factor as the crystalline olivine grains. Based on the fit at this epoch at 2.8 AU, where there is full far-IR spectra coverage, the model fits at other epochs are also constructed assuming the “hot” crystal model.

4.2. 1997 February UT

For this epoch (preperihelion), the best-fit model SED ($\chi^2_v = 16.36$) is reproduced by co-adding a 5770 K blackbody (reflected solar spectrum) and a thermal model flux spectrum using a grain size distribution (slope $N = 3.7$) that peaks at $a_p = 0.2\ \mu\text{m}$ ($M = 3.7$) and a high fractal dimension for the amorphous materials of $D = 2.5$ (Fig. 7). Note that the model SED predicts values greater than the 18.3 μm photometry point. This large discrepancy at 18 μm could be

due to the crystals being warmer than the “hot crystal” model at this heliocentric distance or to the uncertainty in the flux value of the data point being larger than the formal error by a factor of 4, as presented by Williams et al. (1997).

4.3. 1997 April UT

The best-fit synthetic model SED for the 1997 April 11 UT epoch (near perihelion) was derived by co-adding the 5770 K blackbody to a thermal model flux spectrum calculated using a grain size distribution, with slope $N = 3.7$, that peaks at $a_p = 0.2\ \mu\text{m}$ ($M = 3.7$), with a fractal dimension for the amorphous materials of $D = 2.5$ (Fig. 8). The reduced χ^2 of the fit is $\chi^2_v = 99.75$, which is significantly larger than at other epochs because the relative photometric uncertainty of the HIFOGS spectral data are small ($S/N \gtrsim 100$), highly constraining the model through the 7.5–13.5 μm region.

For this epoch only, the $1\ \sigma$ uncertainties in the fit parameters are determined experimentally from the shape of the multidimensional χ^2 ellipsoid, by finding where the sides of the χ^2 ellipsoid begin to grow rapidly from the relatively flat-bottomed portion of the multidimensional surface. The parameter pairs amorphous pyroxene and amorphous olivine and crystalline olivine and amorphous olivine are the strongest pairwise correlations. Therefore, these two pairs of parameters are used to experimentally define $\Delta\chi^2$ for 1997 April UT; a $\Delta\chi^2$ -value of 200 is found to encompass

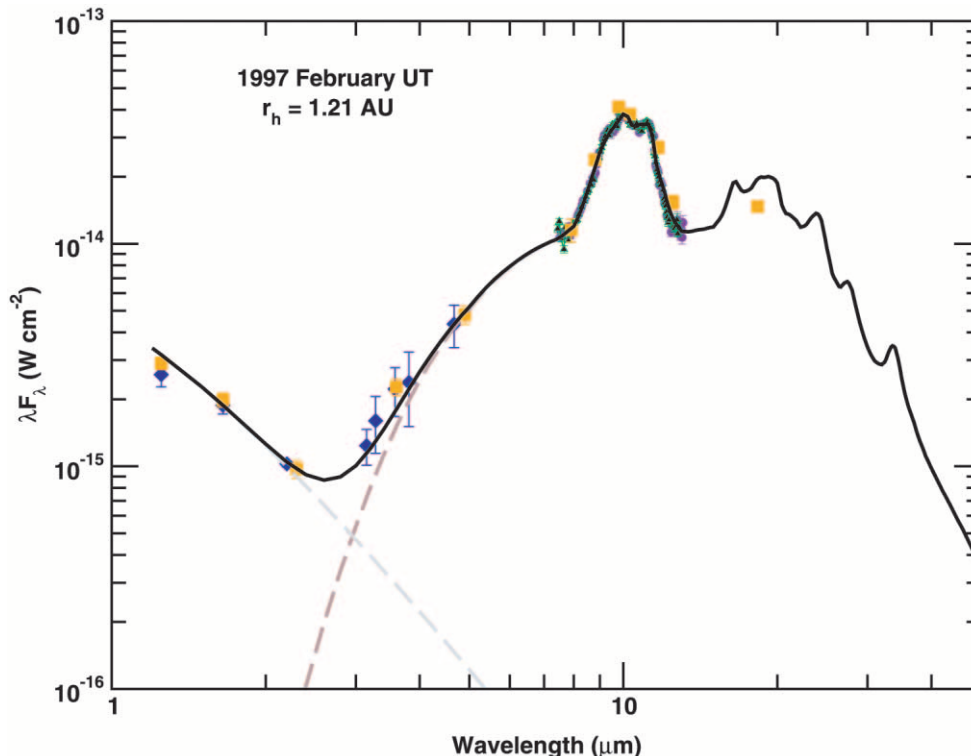


FIG. 7.—Model SED of Hale-Bopp, compared with the observed SED for 1997 February UT. The SED is constructed from data points from HIFOGS spectrophotometry (1997 February 14 UT, violet circles; 1997 February 15 UT, green triangles), synthetic-aperture photometry from URCAM imaging (1997 February 10 UT, blue diamonds), and photometry from Williams et al. (1997; 1997 February 20 UT, orange squares). A synthetic spectral model fit (black line) is constructed from a 5770 K blackbody (dashed gray line) and the calculated thermal model (dashed brown line). This synthetic model is fitted to the SED with $\chi^2_v = 16.36$ and parameters $N = 3.7$, $M = 3.7$ ($a_p = 0.2\ \mu\text{m}$), and $D = 2.5$. The abundances by number at the peak of the grain size distribution are listed in Table 3.

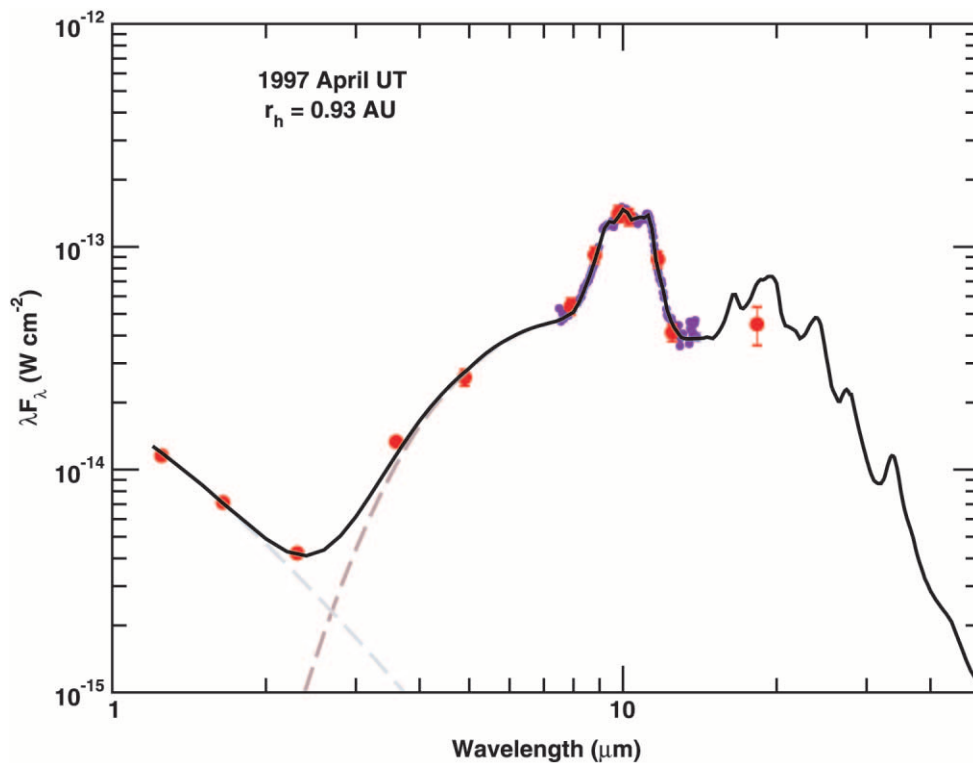


FIG. 8.—Model SED of Hale-Bopp, compared with the observed SED for 1997 April UT. The SED is constructed from data points from HIFOGS spectrophotometry (1997 April 11 UT, *violet circles*) and photometry from Mason et al. (2001; statistically weighted average of 1997 April 9 and 14 UT data points, *red circles*). A synthetic spectral model fit (*black line*) is constructed from a 5770 K blackbody (*dashed gray line*) and the calculated thermal model (*dashed brown line*). This synthetic model is fitted to the SED with $\chi^2 = 99.75$ and parameters $N = 3.7$, $M = 3.7$ ($a_p = 0.2 \mu\text{m}$), and $D = 2.5$. The abundances by number at the peak of the grain size distribution are listed in Table 3.

the lowest and flattest part of the χ^2 multidimensional ellipsoid for correlated parameters. Thus, the errors associated with the parameters are the correlated errors within our empirically determined confidence level.

The fractal dimension and peak of the grain size distribution for the 1997 April UT epoch are the same as those for the 1997 February UT epoch. The 1997 April UT model SED is too high compared to the $18.3 \mu\text{m}$ photometry point. The poor fit at $18.3 \mu\text{m}$, compared to the fit at shorter wavelengths for 1997 April UT, is comparable to that of 1997 February UT and might be attributable to similar causes.

4.4. 1997 June UT

The best-fit synthetic model SED for this epoch (postperihelion) was generated by co-adding the 5770 K blackbody and the thermal model flux spectrum calculated using a grain size distribution (slope $N = 3.5$) that peaks at $a_p = 0.2 \mu\text{m}$ and a fractal dimension for the amorphous materials of $D = 2.6$ (Fig. 9). The fractal porosity for the 1997 June UT epoch is higher (i.e., less porous grains) than that of the 1997 February and April UT epochs. The grain parameters imply that the porous grains are not as dominant as they were while the comet was close to perihelion and that the coma was populated with grains similar to those seen preperihelion, during the 1996 October UT epoch. The implications of these changes in the grain properties with heliocentric distance are discussed in § 5. Finally, as with the 1997 February and April UT epochs, the $18.3 \mu\text{m}$ data point is poorly fitted by the model SED.

5. DISCUSSION

5.1. The r_h Evolution of Amorphous Grains from SED Modeling

The models (§ 4) suggest that the physical properties of the dust grains and the relative abundances of the materials in the coma of Hale-Bopp changed with heliocentric distance. First, as the comet approached perihelion, the analysis indicates that there is (1) a drop in the amount of flux from large amorphous grains ($\geq 5 \mu\text{m}$ radii), (2) an increase in the fractal porosity of these large amorphous grains, and (3) an increase in the contrast of $9.3 \mu\text{m}$ crystalline orthopyroxene resonance peak with respect to the strong, broad, amorphous silicate resonances. Second, the subsequent reversal of these changes was witnessed postperihelion, as the comet increased its heliocentric distance.

On the other hand, there are some grain properties that remained relatively constant with r_h . The grain radius at which the grain size distribution peaks is $a_p = 0.2 \mu\text{m}$ at all epochs. The relative abundance by mass of submicron-sized crystalline olivine and crystalline orthopyroxene grains, relative to the total number of submicron-sized grains, increased by only 20% close to perihelion. Therefore, at all epochs, the submicron-radii silicate grains are generally a mixture of 70% amorphous and 30% crystalline grains. By mass, the total silicate (amorphous and crystalline) to carbon ratio is ~ 4 , significantly smaller than the ratio of ~ 40 determined for comet Halley (Krishna Swamy et al. 1988).

In 1996 October UT, at 2.8 AU preperihelion, the measured $10 \mu\text{m}$ flux from Hale-Bopp is dominated by small, moderately porous, amorphous silicate grains (a $1 \mu\text{m}$

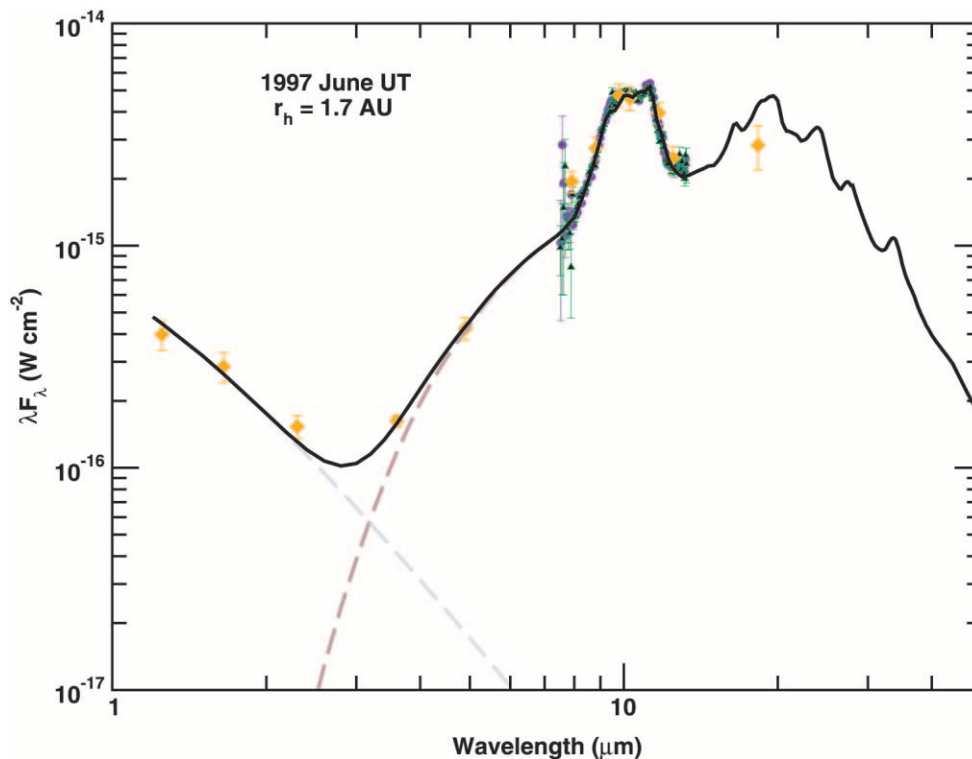


FIG. 9.—Model SED of Hale-Bopp, compared with the observed SED for 1997 June UT. The SED is constructed from data points from HIFOGS spectrophotometry (1997 June 24 UT, *violet circles*; 1997 June 25 UT, *green triangles*), and photometry from Mason et al. (2001; statistically weighted average of 1997 June 9 and 10 UT data points, *orange squares*). A synthetic spectral model fit (*black line*) is constructed from a 5770 K blackbody (*dashed gray line*) and the calculated thermal model (*dashed brown line*). This synthetic model is fitted to the SED with $\chi^2 = 7.48$ and parameters $N = 3.7$, $M = 3.7$ ($a_p = 0.2 \mu\text{m}$), and $D = 2.7$. The abundances by number at the peak of the grain size distribution are listed in Table 3.

radius amorphous grain is 20% porous). Also, there is a significant contribution to the flux from larger grains with low porosity (a $10 \mu\text{m}$ radius amorphous grain is 40% porous; § 4.1). Large particles are thought to originate on the surface, becoming entrained in the gas outflow (Shoshany et al. 1999). Large, highly porous grains ($\geq 80\%$ vacuum) dominate the emission over the large, less porous grains (less than 68% vacuum) of the same radii (Xing & Hanner 1997). Highly porous grains would have been easily detected if they were present in the coma. Thus, the highly porous grains present at smaller heliocentric distances are not present in appreciable numbers at this heliocentric distance. The slope of the grain size distribution at this epoch is well constrained to $N = 3.4$, close to the slope of the interstellar power law of $N = 3.5$ (Mathis, Rumpl, & Nordsiek 1977).

Near perihelion, changes in the grain properties that are required to fit the measured HIFOGS data, as well as the SEDs, include an increase in the fractal porosity (1 and $10 \mu\text{m}$ grains contain 70% and 90% vacuum, respectively) and an increase in the slope of the grain size distribution to $N = 3.7$. The slope of the grain size distribution is in the range determined for other comets (§ 5.5). In Hale-Bopp's coma, the particles in the arcs formed by the jets contain grains smaller than in those between the arcs, as evidenced by their hotter relative temperatures (HHS) and by their higher polarization (Jones & Georz 2000). These small grains contribute to a strong NIR excess (DiSanti et al. 1999) and to a significant increase in the mid-IR continuum flux (Wooden et al. 1999) above that predicted by the $r_h^{-4} \Delta^{-1}$ relation (Georz & Ney 1992). Therefore, close to

perihelion there are more smaller grains being produced (Table 3; HHS; Williams et al. 1997). As for the less porous large grains, they might have existed in the coma near perihelion, but were not seen because of the high flux from the more porous grains.

During 1997 June UT, when the comet was observed postperihelion at a heliocentric distance of 1.7 AU, the large, less porous grains once again began to dominate the thermal emission. As the comet recedes from the Sun, the fractal dimension of the porous grains begins to revert toward its value at 2.8 AU (preperihelion in 1996 October UT).

5.2. The Presence of “Hot,” Mg-rich Silicate Crystals

Nonporous, small ($\leq 1 \mu\text{m}$) crystalline grains, analogous to those in CPIDPs, adequately model the crystalline resonance features at each temporal epoch. The “hot” silicate crystals are 1.9 times hotter than the radiative equilibrium temperatures calculated for the pure Mg amorphous grains of the same mineral composition. By mass, the submicron-sized crystalline silicates make up 30%–38% of the silicates in Hale-Bopp. The abundances of silicate crystals relative to the total grain population are constrained by the model analysis to be nearly constant at all epochs, with a slight increase close to perihelion (see Table 4).

5.2.1. Plausible Causes for “Hot” Silicate Crystals

The modeling requires that the silicate crystals are “hot.” This model result suggests that “hot” crystals are either

part of some aggregate that warms them, or that the crystalline silicates contain a small amount of Fe and are not pure Mg crystals. The crystalline olivine resonance peak at $11.2 \mu\text{m}$ evident in the spectra implies a high Mg content of $x = y \geq 0.95$ (Jäger et al. 1998). This high Mg content is consistent with the most primitive, highest Mg content ($y \geq 0.95$) materials found in CPIDPs and AMMs (Bradley et al. 1999b) and in Halley pyroxene and olivine grains (clusters C and D in Table 2 of Schulze et al. 1997). Therefore, based on the location of the crystalline resonance features, the crystals are not “hot” as a result of an increased Fe content.

The crystals producing the resonances are not themselves aggregates of crystals, because the wavelengths of their peak resonances require isolated crystals. Yanamandra-Fischer & Hanner (1999) modeled the emission from single and aggregate (with 2 and 5 constituents) tetrahedral-shaped grains of crystalline olivine. For the single grain, the signature crystalline olivine “ $11.2 \mu\text{m}$ ” resonance feature peaks at $11.2 \mu\text{m}$. The “solid” aggregates (30% overlap between constituents) produced a resonance peak $\sim 11.13 \mu\text{m}$, while the “fluffy” aggregates (10% overlap of the constituents) produced a resonance that peaked at a shorter wavelengths ($\leq 11.1 \mu\text{m}$). The crystalline olivine resonance is sharpest in the 1997 April 11 UT HIFOGS spectra, with a peak wavelength of $11.175 \pm 0.045 \mu\text{m}$ based on only a single grating setting (Wooden et al. 1999). Thus, the crystalline resonances are probably not produced by fluffy aggregates of crystals. The inferred crystal grain size distribution in comet Hale-Bopp peaks at $a_p = 0.2 \mu\text{m}$ and is truncated at $1 \mu\text{m}$. These small crystalline grains are consistent with the size of the constituents of CPIDPs of probable cometary origin. Thus, based on the grain size distribution, some of the crystals are probably isolated solid particles.

As a final possibility, an absorbing organic mantle (as proposed by Greenberg & Hage 1990) around the crystals could warm them to the temperatures calculated from our modeling. To produce a resonant feature in amorphous silicates to match the emission from Hale-Bopp, Li & Greenberg (1998) made their large bird’s nest aggregates very porous ($\sim 98\%$). Furthermore, it is unknown what the effect of an absorbing organic mantle has on the resonance features from the crystals. Calculations of aggregate grains with crystals are not tractable at this time. Calculations are needed to determine the amount of organic material needed to heat individual crystals to the temperatures that match the observations.

5.2.2. Increasing Contrast in Orthopyroxene Crystals near Perihelion

Near perihelion, the $9.3 \mu\text{m}$ crystalline orthopyroxene resonance grew, in contrast to the broad amorphous features. At perihelion (0.93 AU), the temperatures of crystalline olivine and crystalline orthopyroxene are modeled to be ~ 220 and ~ 320 K, respectively. The temperature difference between the crystalline olivine and the crystalline orthopyroxene is sufficient to make the abundance of orthopyroxene crystals increase in contrast to the other mineral species near perihelion. The relative abundance of the crystalline olivine to orthopyroxene crystals is 5:1 at 2.8 AU and decreases to 3.8:1 at 0.93 AU.

The olivine crystals are cooler than the orthopyroxene crystals, a model result opposite to the empirical determina-

tion by Wooden et al. (1999) based on Lucey (1998) optical constants. At 0.93 AU, the crystalline olivine radiative equilibrium temperature (220 K) is cooler than either the blackbody temperature (~ 290 K) assigned by HHS or the measured $10 \mu\text{m}$ continuum temperature (~ 410 K) assigned by Wooden et al. (1999) to the crystalline olivine. The crystalline orthopyroxene radiative equilibrium temperature (320 K) also is hotter than the empirical temperature (245 K) determined by Wooden et al. (1999) for the crystalline orthopyroxene. Thus, the radiative equilibrium model analysis indicates that crystalline olivine is more abundant relative to crystalline orthopyroxene. Even so, orthopyroxene crystals are still an important crystalline silicate in comet Hale-Bopp. Pyroxenes are also a significant mineral component of comet Halley, as shown by the reanalysis of Halley’s in situ mass spectrometer measurements (clusters C and D in Table 2 of Schulze et al. 1997).

Only the HIFOGS mapping of the coma near perihelion revealed any differences in the ratio of olivine to orthopyroxene crystals, and only in the sunward direction. Figure 10 shows the spectra centered on the nucleus and offset $5''$ in the sunward direction. Model fits to the sunward spectrum suggest that the peak of the size distribution is the same as that observed toward the nucleus ($a_p = 0.2 \mu\text{m}$). However, the derived mineralogy differed. Crystalline olivine is increased by 29% and crystalline orthopyroxene is increased by 43%, while amorphous olivine is decreased by 35% and amorphous pyroxene and amorphous carbon are decreased slightly, by $\sim 13\%$. The crystalline olivine-to-crystalline orthopyroxene ratio decreases from 3.7 in the nucleus to 3.3

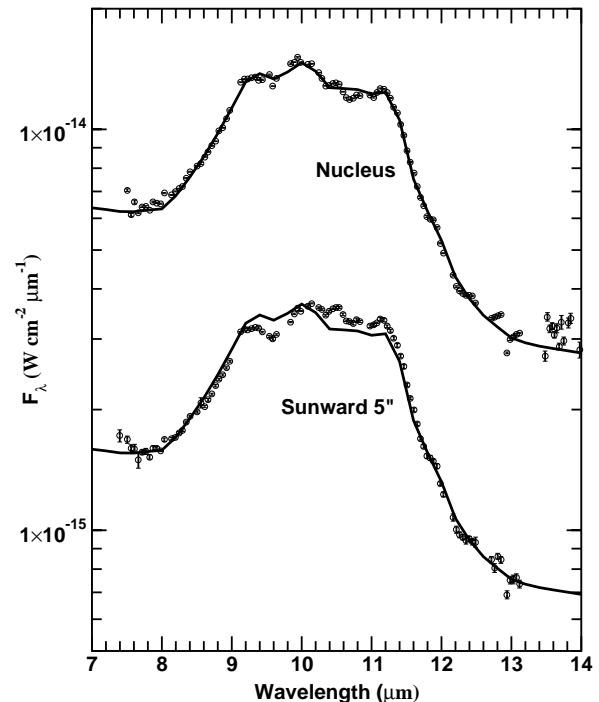


FIG. 10.—Model flux spectra of Hale-Bopp (curves), compared with the HIFOGS spectra (circles) obtained on 1997 April 11 UT ($r_h = 0.93$ AU) on the nuclear region and offset $5''$ sunward ($3'5$ S, $3'5$ W). Overlaid on each spectrum is the 1997 April UT best-model fit. The model spectrum uses fractal porous grains ($D = 2.5$) calculated using the Hanner size distribution, with $N = M = 3.7$, which corresponds to a peak grain size of $a_p = 0.2 \mu\text{m}$. For the $5''$ offset spectrum, the model fit has been scaled down by a factor of 4 to fit the observed flux.

in the sunward direction. The increase in the orthopyroxene crystals by 43% in the sunward direction supports the concept that the 9.3 μm emission is a combination of crystalline orthopyroxene (9.3 μm peak) and amorphous pyroxene (9.3 μm shoulder), as discussed further in § 5.5. Also, the increase in crystalline silicates sunward is in the direction of strong jet activity, supporting the idea that these grains might be dredged up from deep within the nucleus, rather than being lifted off the surface of the comet, as discussed below.

5.3. Hypothesis for r_h -dependent Grain Properties

The coma of Hale-Bopp contained a large reservoir of small ($\leq 0.5 \mu\text{m}$) grains (Williams et al. 1997; Hanner et al. 1999). This small grain reservoir increased as the comet's heliocentric distance decreased, and it is demonstrated in the models by a steepening of the grain size distribution. In addition, the fractal porosity of large, amorphous grains also increased close to perihelion. Higher porosity grains are hotter than lower porosity grains of the same grain radii, and the hotter grains dominate the flux. Highly porous grains could have dominated the emission, but are not detected in appreciable numbers at large heliocentric distances ($r_h \approx 2.8 \text{ AU}$). Highly porous grains only appear in the coma near perihelion ($\lesssim 1.5 \text{ AU}$).

The model analysis leads to two hypotheses: either dust grains ejected by the jets into the coma contain amorphous grains of greater porosity (i.e., material is being dredged up from inside the nucleus), or the dust grain properties in the coma are modified by some mechanism (e.g., fragmentation) that increases the grain porosity and releases crystals. DiSanti et al. (1999) suggest that the strong NIR continuum at $r_h \lesssim 1.5 \text{ AU}$ is a consequence of grain fragmentation. The modeling of the SEDs suggests that the entire grain size distribution steepens at $r_h \lesssim 1.2 \text{ AU}$ and that the grain porosity increases. That is, there are more (by number) smaller grains, and the grains are more porous. Insolation can create areas of large gas and dust production. In Hale-Bopp these jets acted like sprinkler heads as the nucleus rotated, with a mean period of $\sim 11.3 \text{ hr}$ (Sarmecanic et al. 1997; Schleicher et al. 1997; Licandro et al. 1998; Jorda et al. 1999), expelling large amounts of dust into the coma. The change in the grain properties near perihelion might be a consequence of the delivery of grains from within the nucleus into the coma by strong jet activity. Thus, the grain properties near perihelion might be representative of early solar nebula grains.

5.3.1. Release of Porous Particles from Nucleus

Recent modeling of comet nuclei reveals that the comet nucleus itself is very porous and that nuclear pore size increases with decreasing heliocentric distance (Shoshany et al. 1999). Generally, pores free small grains from a fairly thick layer below the surface of the comet. For Hale-Bopp, the effective maximal dust grain size is computed to be 10 μm , based on a computed pore size of $\sim 100 \mu\text{m}$ and a crystalline ice layer of thickness $\sim 1\text{--}4 \text{ m}$ (Prialdnik 1999). The crystalline ice layer is significantly thinner than that deduced for other comets, but thicker than that expected for a new comet. This is consistent with the small number of perihelion passages experienced by Hale-Bopp (Marsden 1999). As the comet approaches perihelion, gas pressure increases the size of the nuclear pores in regions where large amounts

of gas are being generated (i.e., jets). Particles could be liberated from deep inside the comet, altering the observed grain size distribution. These larger particles from deep within the nucleus are likely to be more pristine and more closely resemble the composition of the early solar nebula than those released from the surface.

As the jet activity on the nucleus begins to subside, the pores decrease in size with the decrease in gas pressure. Therefore, the amount and size of dust grains being liberated from inside the nucleus decreases. The pore sizes change with time as ice around the pore is melted (Shoshany et al. 1999). A decrease in the solar insolation results in the pores closing or becoming clogged with icy material. Gas can still pass through pores of any size, but the dust will only pass through those pores large enough for the grains to escape (Shoshany et al. 1999). Closing of cometary pores is a plausible reason for the comet's exhibiting such a dramatic decrease in postperihelion dust production (Wooden et al. 1999, 1997), but not in gas production, and for the reversion of grain porosity toward large heliocentric distance, preperihelion values.

5.3.2. Fragmentation of Grains in the Coma

Fragmentation of larger grains into smaller grains could both steepen the grain size distribution and increase grain porosity. Grains can become fragmented through such mechanisms as collisions. Jones et al. (1994) showed that, given a population of porous and solid grains, processes such as collisions will tend to destroy solid grains, rather than the more porous grains. In the coma, the more porous grains will tend to outlive less porous grains. Let us consider grains to be aggregates of small ($\lesssim 0.2 \mu\text{m}$ radii) particles. If the aggregates are cohesive, they act as a "large" particle. On the one hand, the breakup of such an aggregate into smaller pieces would actually decrease the overall porosity of the grain population. However, this is not what we see in our models of Hale-Bopp. On the other hand, if the aggregates break apart by losing small particles or constituents, then they can be considered an effectively more "porous" particle if the grains retain the large collecting area while becoming deficient of material. Therefore, the large aggregates become more loosely "stuck" together. Grains from the surface of the comet might have already been exposed to UV radiation or a significant high-energy particle flux from the solar wind and become "carbonized," making them far more cohesive (Strazzulla & Baratta et al. 1992 and references therein) and less likely to fragment than nonirradiated grains from the interior. Interior grains at smaller heliocentric distances are likely candidates for fragmentation and therefore could become highly porous.

5.3.3. Possibility of Organics in the Dust

At small heliocentric distances ($r_h \lesssim 1.5 \text{ AU}$), a strong, distributed source of CO (possibly associated with organic materials in the dust) has been detected at a significantly larger spatial distribution than the $1/r$ falloff of the coma material (gas and dust) inferred from IR observations (DiSanti et al. 2001). The source of the distributed CO might be associated with organic materials within the dust (DiSanti et al. 1999). Other molecules, including HNC, CN, C_2 , and H_2CO , can also come from complex organics in the nucleus (Rodgers & Charnley 2001). The sublimation of an organic polymeric "glue," such as polyoxymethylene (POM),

might have led to the fragmentation of grain aggregates in comet Halley's coma (Bönnhardt, Fechtig, & Vanýsek 1990). If dissociation of organic materials in the dust (e.g., materials analogous to aliphatic compounds, identified in IDPs by Brownlee et al. 2000, or POM, as noted by Cottin et al. 2000) is the source of the CO, then the organics in the dust can serve as further evidence of pristine grains dredged up from the nuclear interior near perihelion.

Using the spectral synthesis modeling tools, pure water ice, dirty water ice, CO ice (Quirico & Schmitt 1997), and some organic materials (e.g., tholin; Khare et al. 1984) were incorporated into the grains using Bruggeman mixing theory. The evaporation of these materials from 2.8 to 1.2 AU might have explained the evolution of the grain size distribution and porosity. However, these materials produced strong resonances not present in the spectral data. We are not able to suggest what organic material could produce the distributed source of CO or, when released from the dust, could increase the grain porosity.

We suggest that near perihelion ($r_h \lesssim 1.5$ AU), highly porous, large grains are released from greater nuclear depths. Possibly, the subsequent fragmentation of these particles steepens the grain size distribution and further increases grain porosity.

5.4. Relating Hale-Bopp's Grains to CPIDPs

The closest samples to comet grains are CPIDPs collected from the Earth's stratosphere. CPIDPs are believed to be comet grains, based on their high velocities ($v \geq 16$ km s⁻¹) and eccentric orbits (Brownlee et al. 1995). CPIDPs are distinguished from other IDPs by their chondritic composition, low density, high porosity, lack of layer-lattice silicates (Bradley et al. 1992), and the high Mg content of their crystals ($y \simeq x \gtrsim 0.95$; Bradley et al. 1999b). CPIDPs are aggregates of GEMS (Bradley et al. 1997) and both an amorphous carbon- and an aliphatic-rich carbonaceous matrix (Brownlee et al. 2000). GEMS are Mg-rich, amorphous silicate spherules (≈ 0.1 μ m in size) that contain Fe/Ni and FeS nanoparticles. CPIDPs are dark particles (highly absorbing at visible wavelengths) because of their Fe/Ni nanoparticles, and not because of their carbonaceous matrix (Brownlee et al. 2000). Despite the phase separation of the Mg into the amorphous silicates and the Fe into Fe/Ni nanoparticles, GEMS-rich CPIDPs have spectra well matched to the interstellar absorption feature (Bradley et al. 1999c). The interstellar absorption feature could arise from Fe-bearing amorphous olivine (Li & Greenberg 1997) or from a continuous distribution of ellipsoidal Fe-bearing amorphous pyroxene (Demyk et al. 1999). Thus, modeling Hale-Bopp's amorphous silicates by Fe-bearing, chondritic composition ($x = y = 0.5$), amorphous olivine and amorphous pyroxene grains is the best approach now, even though the recent laboratory research shows that the Mg- and Fe-bearing mineral phases are separated in CPIDPs.

Isotopic measurements of CPIDPs yield evidence of the existence of presolar silicates (Messenger, Keller, & Walker 2002). However, only one of the approximately 30 silicates identified in the IDPs as being presolar (by its ¹⁶O/¹⁷O ratio) is identified mineralogically as forsterite (a pure Mg olivine crystal). In addition to the oxygen isotopic measurements, many CPIDPs contain extremely high deuterium enrichments ($\delta D \sim +2700$ parts per million) on micron and sub-micron size scales. The partial preservation of presolar

molecules, i.e., a D-rich carbonaceous phase, as well as the existence of presolar silicates, supports the pristine nature of CPIDPs.

The composite nature of CPIDPs can serve to diminish the sharper crystalline structures, in contrast to the broad amorphous features (Brownlee et al. 2000). Spectra of whole CPIDPs reveal weak resonances at 9.3, 10.5, and 11.2–11.4 μ m, attributable to Mg-rich pyroxene and olivine crystals (Bradley et al. 1999a, 1999c). These resonances are small deviations from the amorphous silicate resonances. However, when these particles are ultramicrotome thin-sectioned, the crystalline resonances show up in much greater contrast than in the bulk particles (Molster et al. 2001; Bradley et al. 1999c). Despite the lack of a direct spectral comparison of the same particle prior to and after thin-sectioning, the contrast of the crystalline resonances appear to be diminished when these crystals are part of larger aggregates. Few published spectra of CPIDPs have crystalline resonances with as strong a contrast as is evident in Hale-Bopp's 10 μ m feature. Hale-Bopp's strong 10 μ m silicate feature and high-contrast crystalline resonances suggest that Hale-Bopp's aggregates are smaller than those present in other comets or CPIDPs collected in the stratosphere.

The most fragile CPIDPs are those pyroxene-rich CPIDPs that shatter into a cluster of smaller pieces upon impact with the collector; these are the so-called cluster IDPs. The spectra of pyroxene-rich cluster IDPs best match the spectra of comet Hale-Bopp (Wooden et al. 2000a). Cluster IDPs are extremely porous, highly fragile, contain Mg-rich crystalline material, and represent some of the most pristine particles in the solar system (see Wooden, Harker, & Woodward 2000b for a summary of their pristine qualifications). From the CPIDP spectra in the literature, it can be inferred that if crystals are parts of aggregate grains, then the smaller the aggregate grains (analogous to thin sections), the more distinguishable will be the crystalline resonances. Hopefully, future laboratory work will emphasize comparing the spectra of CPIDP particles with the spectra of thin sections of the same CPIDP. This laboratory work is a critical part of spectroscopically assessing the crystalline content of aggregate particles. Computing the heating of crystals as parts of aggregates is also an important avenue of future work. The porous, GEMS-rich component of CPIDPs might serve to warm the poorly absorbing Mg-rich crystals by their contact with the more absorbent silicate materials made dark by the Fe/Ni inclusions in GEMS (Brownlee et al. 2000).

5.5. Comparison with Other Grain Models for Hale-Bopp

Other investigators have modeled the emission from dust grains in Hale-Bopp's coma. The epochs of the observations modeled either coincide with or are within two weeks of the HIFOGS epochs. While our results are similar to the findings of these other investigators, our results differ in that we determine the temperature of the crystalline silicates (and thereby create the "hot" crystal model) using the 1996 October UT SED, model a distribution of grain porosities, and constrain the peak of the grain size distribution using the flux in the 3–5 μ m region, which includes both the thermal and scattered light from the dust grains. Without taking into account the scattered light, model fitting to the thermal NIR SED yields a different peak grain size and grain porosity. For example, we find that for 1997 April UT, using the

approximation that the scattered light is from grains of approximate size of the wavelength (§ 3), at $3.6 \mu\text{m}$ the scattered light accounts for 3% of the measured flux.

Williams et al. (1997) computed a model fit of the photometry points at $\lambda = 3\text{--}5 \mu\text{m}$, using a grain size distribution of solid grains that peaks at $a_p = 0.15 \mu\text{m}$ for the 1997 February UT epoch. In contrast, our fits show that a good match to the SED requires a size distribution of porous grains that peaks at larger grain radii; a_p cannot be smaller than $0.2 \mu\text{m}$ for a fit that includes fractal, porous grains.

HHS examine spectra obtained on 1997 March 28 UT at $3\text{--}5$ and $7\text{--}13 \mu\text{m}$. They use a model consisting of a size distribution of amorphous carbon grains whose flux spectra are computed using Mie theory plus submicron silicate grains whose flux spectra are computed using laboratory-measured emissivities, with the silicate grains assigned a blackbody temperature corresponding to the heliocentric distance of the observation epoch.

The thermal spectral models of HHS are similar to our models in that both models compute the emission spectra of hot, submicron, amorphous carbon grains that are the primary flux contributor to the NIR excess and mid-IR pseudocontinuum. This pseudocontinuum is also attributed to carbon grains by Wooden et al. (1999). HHS find that the best fit to the spectra of the nuclear region on 1997 March 24 UT uses the Hanner grain size distribution with a minimum grain size of $a_0 = 0.05 \mu\text{m}$, a slope of $N = 3.7$, and a peak grain size of $a_p = 0.13 \mu\text{m}$. By fitting the thermal grain model to NIR spectra of Hale-Bopp without including a scattered-light component, HHS derive a smaller peak grain size, which produces model fits outside our 1σ uncertainties.

To fit the $9.3 \mu\text{m}$ feature near perihelion, HHS use pure Mg amorphous pyroxene grains and pyroxene-rich IDPs in an emissivity ratio of about 3.5 : 1. Given their assumption that the mineral components have similar sizes and temperatures, their results are that the most abundant silicate is amorphous pyroxene ($\sim 40\%$) and that the pyroxenes together constitute about two-thirds of the submicron-sized silicates, with $\sim 20\%$ crystalline olivine and $\sim 15\%$ amorphous olivine constituting the other one-third of the submicron silicate grain mineralogy. We use a size distribution of $0.1\text{--}100 \mu\text{m}$ Fe-bearing amorphous pyroxene grains ($x = 0.5$) and $0.1\text{--}1.0 \mu\text{m}$ Mg-rich crystalline orthopyroxene grains in a ratio, by number, of approximately 2 : 1. Overall, at each epoch, we find equal mixtures of pyroxene and olivine minerals. The notable exception is during 1996 October, when we find that the olivines outnumbered the pyroxenes by a ratio of 1.6 : 1. HHS use pyroxene IDPs “Spray 1” and “Key” in their modeling. A fraction of the pyroxene IDP mass is in pyroxene crystals (Bradley et al. 1992, 1999b). The mass fraction required for an IDP aggregate to show the $9.3 \mu\text{m}$ resonance probably depends on the size of the IDP aggregate (§ 5.4). HHS attribute the $9.3 \mu\text{m}$ feature solely to amorphous pyroxene. We attribute the $9.3 \mu\text{m}$ feature to a combination of amorphous pyroxene and crystalline orthopyroxene.

Finally, HHS find that fits to their 1997 February 19 and 1997 March 24 UT data sets yield the same relative abundances of silicate minerals at both epochs, in the nuclear region and in the jet-produced arcs. However, in the 1997 April 11 UT HIFOGS data set, an increase in the amount of pyroxene silicates is found in the region offset sunward from

the nucleus $5''$. Despite the differences between these two models, both models demonstrate that Hale-Bopp contained a large number of submicron-sized grains and that a large percentage of these grains are of pyroxene mineralogy.

Li & Greenberg (1997) use a model altogether different to fit the photometry points at $3\text{--}20 \mu\text{m}$ from 1997 February 20 UT. Their grains consist of amorphous silicate cores surrounded by organic refractory mantles. These organic mantles are orders of magnitude more absorptive than amorphous carbon and Fe-bearing amorphous silicates. Therefore, their strongly absorbing model grains are very hot compared to absorbing particles modeled by other investigators. Li & Greenberg’s grains are required to be very large and highly porous to produce model spectra that exhibit a $10 \mu\text{m}$ silicate feature, as well as grains cool enough to produce the required $3\text{--}5 \mu\text{m}$ continuum. A single porosity is assigned to grains of every size, unlike the fractal porosity used in the modeling, which assigns a higher porosity to grains of larger size. They found that by using $\sim 97\%$ porous grain aggregates composed of amorphous olivine cores coated with organic residues, the Hanner grain size distribution produced a good fit to the data at a peak size of $a_p \sim 25 \mu\text{m}$, significantly larger than the models previously discussed. To examine the contribution from crystalline silicates, they add the emission from bare (i.e., no organic mantle), isolated, submicron crystalline grains into their model. They find acceptable fits when assuming that the crystal grains composed between 25% and 50% of the silicates by mass. However, they did not have the spectral resolution to uniquely determine the fit. We find similar relative masses ($\sim 30\%\text{--}\sim 40\%$) of crystalline silicates, depending on the heliocentric distance of comet Hale-Bopp (Table 4).

Brucato et al. (1999) model the spectrum of Hale-Bopp (preperihelion) using the mass extinction coefficients of amorphous carbon, chondritic composition amorphous olivine, and pure Mg crystalline olivine. No amorphous pyroxene is used. Fits to the 1996 October 6 UT ISO SWS $6\text{--}45 \mu\text{m}$ spectrum yield submicron-size grain temperatures of 205 K (all minerals), hotter than the blackbody temperature of 163 K. They include a cooler continuum component, representing emission from larger (greater than $50 \mu\text{m}$), cooler grains ($159 \text{ K} \approx T_{\text{BB}}$), to match the ISO SWS spectrum. Based on their relative number of large ($50\text{--}10^6 \mu\text{m}$) to submicron ($0.01\text{--}1 \mu\text{m}$) sized grains, they estimate the exponent of a power-law grain size distribution to be $N \simeq 2.4$. This power-law grain size distribution is much flatter than derived from other models for Hale-Bopp. Relative mass fractions for the submicron grains are 11% for amorphous carbon, 69% for crystalline olivine, and 20% for amorphous olivine. They find a crystalline-to-amorphous silicate ratio of 3.45 : 1 at 2.9 AU, in contrast to our ratio of 0.5 : 1 at the same heliocentric distance. Brucato et al. also find a large number of silicates compared to carbon (silicate : carbon = 8 : 1).

The differences in the Brucato et al. relative abundances of the grain species result from their assignment of the same temperature to all submicron-sized amorphous carbon, amorphous olivine, and crystalline olivine grains. Their submicron carbon grains are cooler than the submicron silicate grains in our model, and therefore their carbon grains are more abundant, relative to the silicate grains, than in our model. Grain temperatures depend on mineralogy and grain size (§ 3; HHS; Harker 1999). Deriving relative abundances of various mineral species depends on their relative temper-

atures (Hanner et al. 1999; Wooden et al. 1999), and the results of that process must be considered along with the modeling methodology.

5.6. Comparison with Other Oort Cloud Comets and the ISM

Many comparisons have been made between the silicate features measured in Hale-Bopp and those of other comets (Mason et al. 2001; Wooden et al. 2000a; HHS; Wooden et al. 1999). Much of this work tries to identify whether Hale-Bopp is a unique comet in terms of its mineralogy, its grain size distribution, or some combination of both. This is a difficult concept to address, since the makeup of grains in the coma is complicated through such processes as grain fragmentation or nucleus porosity, which can release early solar nebula “nuclear” grains (§ 5.3.1). Whether the grains are “nucleus” or “surface” might be yet another parameter in comparing comets.

HHS applied their model (preserving the mineral mix determined from their fits of the emission of Hale-Bopp) to other comets that exhibited a silicate emission feature. They found that they could achieve a good fit to comet Mueller (C/1993 A1) by varying only the peak of the grain size distribution and the continuum-to-silicate ratio. This implies that Mueller and Hale-Bopp share a similar mineralogy, but a different grain size distribution of the absorbing grains. However, when they fitted the emission from comets 1P/Halley, Levy (C/1990 K1), Bradfield (C/1987 P1), and Kohoutek, they found that the 10 μm feature was broader and flatter than that found in Hale-Bopp near perihelion.

The values for N (i.e., the large grain size slope) used in the models of Hale-Bopp ($N = 3.4\text{--}3.7$) are small compared with those of model spectra computed for other comets (Hanner 1983, 1984). This is in agreement with the idea that most of the thermal emission from Hale-Bopp was primarily from small particles (Williams et al. 1997; Wooden et al. 1999). The value of N used in the SED models is closer to that used for the ISM.

Other long-period comets, such as Wilson 1987 VII and C/1996 Q1 Tabur, show little or no silicate resonance feature. A deficit of submicron silicate grains is the reason for a weak silicate resonance feature. However, it is unclear whether the lack of distinctive crystalline resonance features is due to a deficit of small crystalline grains or to an absence of crystals altogether. Harker et al. (1999) found that a mixture of amorphous and crystalline olivine grains produced a better fit to the emission feature of comet Tabur than amorphous silicates alone. Therefore, it is still too early to make any conclusive statements about the relative mineralogies among comets. It is clear that further observations and analyses need to be conducted to understand how large a role the grain size distributions play in the modeling of emission from cometary silicates, especially from silicate crystals.

6. SUMMARY

Through thermal emission modeling of the SED of comet Hale-Bopp at four distinct temporal epochs pre- and post-perihelion, some properties of the optically dominant coma dust grains have successfully been deduced:

1. The slope (N) of the grain size distribution at large grain sizes steepens ($N = 3.4\text{--}3.7$) as the comet approaches perihelion.

2. A fractal, porous model of the amorphous silicates and amorphous carbon grains must be used for each epoch. As the comet approaches perihelion, the value of the fractal dimension decreases from $D = 2.8$ to 2.5 , implying that the number of fractal porous particles increases. Postperihelion, the fractal dimension increases to $D = 2.7$ as the comet recedes from the Sun.

3. The grain size distribution remains peaked at $0.2 \mu\text{m}$ for each temporal epoch.

4. For the 1996 October UT epoch, the temperature of the crystalline olivine grains is empirically determined to be hotter (by a factor of 1.9) than the temperature determined for pure Mg crystals, using optical constants extrapolated from amorphous olivine. This implies an increase of the UVIS part of Q_{abs} for the crystalline olivine by a factor of 74 to attain such temperatures.

5. The relative abundance of the crystalline olivine to crystalline orthopyroxene crystals is 5:1 at 2.8 AU and decreases to 3.8:1 at 0.93 AU.

6. Throughout Hale-Bopp's perihelion passage, approximately 30% of the submicron-sized grains by mass are silicates.

7. The r_h dependence of the emission from Hale-Bopp can be understood by assuming a porous nucleus model with pore sizes that increase close to perihelion, releasing more particles from the interior of Hale-Bopp via active jets.

D. E. H. acknowledges support from the NRC. D. H. W. acknowledges the support of the NASA Ames Director's Discretionary Fund. C. E. W. acknowledges support from the NSF (AST 94-53354), NASA (GRSP NGT2-52218; NAG5-7906). D. E. H. and C. E. W. acknowledge the IR Group at the University of Rochester and Richard J. Rudy of the Aerospace Corp. D. E. H. also acknowledges the contributions of T. Henning and T. L. Hayward to this project. We also thank the telescope support staff at the NASA IRTF for their assistance during our daytime HIFOGS observations. Finally, the authors thank an anonymous referee, whose comments and suggestion greatly improved the manuscript.

REFERENCES

- Bazell, D., & Dwek, E. 1990, *ApJ*, 360, 142
 Bell, K. R., Cassen, P. M., Wasson, J. T., & Woolum, D. S. 2000, in *Protostars and Planets IV*, ed. V. Mannings, A. P. Boss, & S. S. Russell (Tucson: Univ. Arizona Press), 897
 Bockelée-Morvan, D., Gautier, D., Hersant, F., Huré, J.-M., & Robert, F. 2002, *A&A*, 384, 1107
 Bönhardt, H., Fechtig, H., & Vanýsek, V. 1990, *A&A*, 231, 543
 Bohren, C. F., & Huffman, D. R. 1983, *Absorption and Scattering of Light by Small Particles* (New York: Wiley)
 Bradley, J. P. 1988, *Geochim. Cosmochim. Acta*, 52, 889
 ———. 1994, *Science*, 265, 925
 Bradley, J. P., Brownlee, D. E., & Snow, T. P. 1997, in *ASP Conf. Ser.* 122, *From Stardust to Planetesimals*, ed. Y. J. Pendleton & A. G. G. M. Tielens (San Francisco: ASP), 217
 Bradley, J. P., Humecki, H. J., & Germani, M. S. 1992, *ApJ*, 394, 643
 Bradley, J. P., Keller, L. P., Brownlee, D. E., & Thomas, K. L. 1996, *Meteoritics Planet. Sci.*, 31, 394
 Bradley, J. P., Keller, L. P., Gezo, J., Snow, T., Flynn, G. J., Brownlee, D. E., & Bowey, J. 1999a, *Lunar Planet. Sci. Conf.*, 30, 1835
 Bradley, J. P., Snow, T. P., Brownlee, D. E., & Hanner, M. S. 1999b, in *Solid Interstellar Matter: The ISO Revolution*, ed. L. d'Hendecourt, C. Joblin, & A. Jones (Berlin: Springer), 298

- Bradley, J. P., et al. 1999c, *Science*, 285, 1716
- Bregman, J. D., Campins, H., Witteborn, F. C., Wooden, D. H., Rank, D. M., Allamandola, L. J., Cohen, M., & Tielens, A. G. G. M. 1987, *A&A*, 187, 616
- Brownlee, D. E., Joswiak, D. J., Bradley, J. P., Gezo, J. C., & Hill, H. G. M. 2000, *Lunar Planet. Sci. Conf.*, 31, 1921
- Brownlee, D. E., Joswiak, D. J., Schlutter, D. J., Pepin, R. O., Bradley, J. P., & Love, S. G. 1995, *Lunar Planet. Sci. Conf.*, 26, 183
- Brucato, J. R., Colangeli, L., Mennella, V., Palumbo, P., & Bussoletti, E. 1999, *Planet. Space Sci.*, 47, 773
- Bruggeman, D. A. G. 1935, *Ann. Phys. (Leipzig)*, 24, 636
- Chýlek, P., & Videen, G. 1998, *Opt. Commun.*, 146, 15
- Cottin, H., Gazeau, M. C., Doussin, J. F., & Raulin, F. 2000, *J. Photochem. Photobiol.*, 135, 53
- Crovisier, J., Leech, K., Bockelée-Morvan, D., Brooke, T. Y., Hanner, M. S., Altieri, B., Keller, H. U., & Lellouch, E. 1997, *Science*, 275, 1904
- Demyk, K., Jones, A. P., Dartois, E., Cox, P., & d'Hendecourt, L. 1999, *A&A*, 349, 267
- DiSanti, M. A., Mumma, M. J., Dello Russo, N., & Magee-Sauer, K. 2001, *Icarus*, 153, 361
- DiSanti, M. A., Mumma, M. J., Dello Russo, N., Magee-Sauer, K., Novak, R., & Rettig, T. W. 1999, *Nature*, 399, 662
- Divine, N., & Newburn, R. L., Jr. 1987, *A&A*, 187, 867
- Dorschner, J., Begemann, B., Henning, T., Jäger, C., & Mutschke, H. 1995, *A&A*, 300, 503
- Draine, B. T., & Lee, H. M. 1984, *ApJ*, 285, 89
- Dwek, E. 1985, *ApJ*, 297, 719
- Edoh, O. 1983, Ph.D. thesis, Univ. Arizona
- Elias, J. H., Frogel, J. A., Matthews, K., & Neugebauer, G. 1982, *AJ*, 87, 1029
- Gehrz, R. D., & Ney, E. P. 1992, *Icarus*, 100, 162
- Goetz, J. A., et al. 1998, *ApJ*, 504, 359
- Greenberg, J. M., & Hage, J. I. 1990, *ApJ*, 361, 260
- Grossman, L. 1972, *Geochim. Cosmochim. Acta*, 38, 47
- Grün, E., et al. 2000, *Broadband Infrared Photometry of Comet Hale-Bopp with ISOPHOT* (Heidelberg: MPK)
- Hallenbeck, S. L., Nuth, J. A., III, & Daukantus, P. L. 1998, *Icarus*, 131, 198
- Hanner, M. S. 1983, in *Cometary Exploration*, ed. T. I. Gombosi (Budapest: Hungaria Acad. Sci.), Vol. 2, 1
- . 1984, *Adv. Space Res.*, 4, 189
- . 1988, in *Infrared Observations of Comets Halley and Wilson and Properties of the Grains*, ed. M. S. Hanner (CP-3004; Washington: NASA), 22
- Hanner, M. S., Lynch, D. K., & Russell, R. W. 1994, *ApJ*, 425, 274
- Hanner, M. S., Lynch, D. K., Russell, R. W., Hackwell, J. A., Kellogg, R., & Blaney, D. 1996, *Icarus*, 124, 344
- Hanner, M. S., Veeder, G. J., & Tokunaga, A. T. 1992, *AJ*, 104, 386
- Hanner, M. S., et al. 1985, *Icarus*, 64, 11
- . 1999, *Earth Moon Planets*, 79, 247
- Harker, D. E. 1999, Ph.D. thesis, Univ. Wyoming
- Harker, D. E., Woodward, C. E., Wooden, D. H., Witteborn, F. C., & Meyer, A. W. 1999, *AJ*, 118, 1423
- Hayward, T. L., & Hanner, M. S. 1997, *Science*, 275, 1907
- Hayward, T. L., Hanner, M. S., & Sekanina, Z. 2000, *ApJ*, 538, 428 (HHS)
- Jäger, C., Molster, F. J., Dorschner, J., Henning, T., Mutschke, H., & Waters, L. B. F. M. 1998, *A&A*, 339, 904
- Jewitt, D. 1991, in *IAU Colloq. 116, Comets in the Post-Halley Era*, ed. R. L. Newburn, Jr., M. Neugebauer, & J. Rahe (Dordrecht: Kluwer), 19
- Jones, A. P., Tielens, A. G. G. M., Hollenbach, D. J., & McKee, C. F. 1994, *ApJ*, 433, 797
- Jones, T. J., & Gehrz, R. D. 2000, *Icarus*, 143, 338
- Jorda, L., Rembor, K., Lecacheux, J., Colom, P., Colas, F., Frappa, E., & Lara, L. M. 1999, *Earth Moon Planets*, 77, 167
- Joyce, R. R. 1992, in *ASP Conf. Ser. 23, Astronomical CCD Observing and Reduction Techniques*, ed. S. B. Howell (San Francisco: ASP), 258
- Khare, B. N., et al. 1984, *Adv. Space Res.*, 4, 59
- Koike, C., Shibai, H., & Tsuchiyama, A. 1993, *MNRAS*, 264, 654
- Kozasa, T., Blum, J., & Mukai, T. 1992, *A&A*, 263, 423
- Krishna Swamy, K. S. 1997, *Physics of Comets* (2d ed.; Singapore: World Scientific)
- Krishna Swamy, K. S., Sandford, S. A., Allamandola, L. J., Witteborn, F. C., & Bregman, J. D. 1988, *Icarus*, 75, 351
- Krot, A. N., Scott, E. R. D., & Zolensky, M. E. 1997, *Meteoritics Planet. Sci.*, 32, 31
- Li, A., & Greenberg, J. M. 1997, *A&A*, 323, 566
- Licandro, J., et al. 1998, *ApJ*, 501, L221
- Lien, D. J. 1990, *ApJ*, 355, 680
- Lisse, C. M., A'Hearn, M. F., Hauser, M. G., Kelsall, T., Lien, D. J., Moseley, S. H., Reach, W. T., & Silverberg, R. F. 1998, *ApJ*, 496, 971
- Lucey, P. G. 1998, *J. Geophys. Res.*, 103, 1703
- Marsden, B. G. 1999, *Earth Moon Planets*, 79, 3
- Mason, C. G., Gehrz, R. D., Jones, T. J., Woodward, C. E., Hanner, M. S., & Williams, D. M. 2001, *ApJ*, 549, 635
- Mathis, J. S., Rumpl, W., & Nordsieck, K. H. 1977, *ApJ*, 217, 425
- Maxwell Garnett, J. C. 1904, *Philos. Trans. R. Soc. London*, A 203, 385
- Messenger, S., Keller, L. P., & Walker, R. M. 2002, *Lunar Planet. Sci. Conf.*, 33, 1887
- Molster, F. J., Bradley, J. P., Sitko, M. L., & Nuth, J. A., III 2001, *Lunar Planet. Sci. Conf.*, 32, 1391
- Morfill, G. E., Durisen, R. H., & Turner, G. W. 1998, *Icarus*, 134, 180
- Petrova, E. V. 1999, *Astron. Vestnik*, 33, 260
- Press, W. H., Teukolsky, S. A., Vetterling, W. T., & Flannery, B. P. 1992, *Numerical Recipes* (New York: Cambridge Univ. Press)
- Prialnik, D. 1999, *Earth Moon Planets*, 77, 223
- Quirico, E., & Schmitt, B. 1997, *Icarus*, 128, 181
- Reach, W. T. 1988, *ApJ*, 335, 468
- Rodgers, S. D., & Charnley, S. B. 2001, *MNRAS*, 320, L61
- Rudy, R. J., Rossano, G. S., & Puetter, R. C. 1996, *ApJ*, 458, L41
- Sarmecanic, J., Osip, D. J., Fomenkova, M., & Jones, B. 1997, *IAU Circ.*, 6600, 1
- Schleicher, D. G., Lederer, S. M., Millis, R. L., & Farnham, T. L. 1997, *Science*, 275, 1913
- Schulze, H., Kissel, J., & Jessberger, E. K. 1997, in *ASP Conf. Ser. 122, From Stardust to Planetesimals*, ed. Y. J. Pendleton & A. G. G. M. Tielens (San Francisco: ASP), 397
- Shoshany, Y., Podolak, M., Prialnik, D., & Berkowitz, B. 1999, *Icarus*, 137, 348
- Steyer, T. R. 1974, Ph.D. thesis, Univ. Arizona
- Strazzulla, G., & Baratta, G. A. 1992, *A&A*, 266, 434
- Tielens, A. G. G. M., Waters, L. B. F. M., Molster, F. J., & Justtanont, K. 1997, *Ap&SS*, 255, 415
- van de Hulst, H. C. 1957, *Light Scattering by Small Particles* (New York: Wiley)
- Waelkens, C., Malfait, K., & Waters, L. B. F. M. 1999, *Earth Moon Planets*, 79, 265
- Waters, L. B. F. M., & Waelkens, C. 1998, *ARA&A*, 36, 233
- Waters, L. B. F. M., et al. 1999, *The Universe as Seen by ISO*, ed. P. Cox & M. F. Kessler (ESA SP-427; Garching: ESO), 219
- Weisberg, M. K., Zolensky, M. E., & Prinz, M. 1997, *Meteoritics Planet. Sci.*, 32, 791
- Williams, D. M., et al. 1997, *ApJ*, 489, L91
- Witteborn, F. C., Bregman, J. D., Rank, D. M., & Cohen, M. 1991, in *Proc. of the 1991 North American Workshop on Infrared Spectroscopy*, ed. R. E. Stencel (Boulder: Univ. Colorado), 29
- Wolff, M. J., Clayton, G. C., Martin, P. G., & Schulte-Ladbeck, R. E. 1994, *ApJ*, 423, 412
- Wooden, D. H., Butner, H. M., Harker, D. E., & Woodward, C. E. 2000a, *Icarus*, 143, 126
- Wooden, D. H., Harker, D. E., & Woodward, C. E. 2000b, in *ASP Conf. Ser. 196, Thermal Emission Spectroscopy and Analysis of Dust, Disks, and Regoliths*, ed. M. L. Sitko, A. L. Sprague, & D. K. Lynch (San Francisco: ASP), 99
- Wooden, D. H., Harker, D. E., Woodward, C. E., Butner, H. M., Koike, C., Witteborn, F. C., & McMurtry, C. M. 1999, *ApJ*, 517, 1034
- Wooden, D. H., Harker, D. E., Woodward, C. E., Butner, H. M., Seargent, D. A. J., Aguiar, J. G. D., Lourencon, R., & de Souza, W. C. 1997, *IAU Circ.*, 6741, 2
- Xing, Z., & Hanner, M. S. 1997, *A&A*, 324, 805
- Yanamandra-Fisher, P. A., & Hanner, M. S. 1999, *Icarus*, 138, 107

ERRATUM: “GRAIN PROPERTIES OF COMET C/1995 O1 (HALE-BOPP)” (ApJ, 580, 579 [2002])

DAVID E. HARKER

Center for Astrophysics and Space Sciences, University of California, San Diego

DIANE H. WOODEN

Space Science Division, NASA Ames Research Center

CHARLES E. WOODWARD

Department of Astronomy, University of Minnesota

AND

CAREY M. LISSE

Department of Astronomy, University of Maryland

In our original paper, the parameters for the best-fit model SEDs in Table 3 and the derived mass ratio of the total of submicron-sized grains listed in Table 4 were incorrectly quoted. For comet C/1995 O1 (Hale-Bopp), for the four epochs UT 1996 September/October ($r_h = 2.8$ AU), 1997 February ($r_h = 1.21$ AU), 1997 April ($r_h = 0.93$ AU), and 1997 June ($r_h = 1.7$ AU), the SED model fits shown respectively in Figures 6–9 utilize N_p (crystalline olivine) larger than that quoted in Table 3 of the original paper. We have corrected this error in the revised Table 3 given here. This error was propagated into Table 4, which also used incorrect uniform bulk densities for all minerals in deriving the ratios of submicron grain abundances. A corrected Table 4 is given below, using the corrected bulk density of $\rho_C = 2.5 \text{ g cm}^{-3}$ for carbon grains and of $\rho_{Si} = 3.3 \text{ g cm}^{-3}$ for silicate grains, and taking into account that the submicron amorphous carbon and amorphous silicate grains are porous (model parameter $D < 3$). For the total population of submicron grains, the derived silicate-to-amorphous carbon ratio is in the range of 8.1–13.3, significantly higher than the range of 3.8–4.5 quoted in our original paper. Furthermore, for comet Hale-Bopp the silicate crystalline-to-amorphous ratio spans the range 1.5–3.7, 3 to 4 times greater than the range of crystalline silicate/amorphous silicate = 0.5–0.9 originally quoted by us.

TABLE 3
MODEL PARAMETERS

UT DATE (1)	r_h (AU) (2)	EPOCH (3)	N^a (4)	M^b (5)	D^c (6)	N_p^d					ν^e (12)	χ^2_ν (13)
						Amorphous Pyroxene ($\times 10^{23}$) (7)	Amorphous Olivine ($\times 10^{23}$) (8)	Amorphous Carbon ($\times 10^{23}$) (9)	Crystalline Olivine ($\times 10^{23}$) (10)	Crystalline Pyroxene ($\times 10^{23}$) (11)		
1996 Oct 11–14.....	2.8	Preperihelion	3.4	3.4	2.8	0.14 ± 0.03	0.15 ± 0.02	0.12 ± 0.02	0.30 ± 0.01	0.03 ± 0.01	542	1.70
1997 Feb 14–15	1.21	Preperihelion	3.7	3.7	2.5	2.48 ± 0.10	1.25 ± 0.06	1.23 ± 0.10	3.02 ± 0.05	0.27 ± 0.05	197	16.36
1997 Apr 11.....	0.97	Near perihelion	3.7	3.7	2.5	2.73 ± 0.22	1.78 ± 0.17	2.22 ± 0.10	6.33 ± 0.10	0.86 ± 0.13	125	99.75
1997 Jun 24–25.....	1.7	Postperihelion	3.7	3.7	2.7	1.23 ± 0.07	0.51 ± 0.05	0.78 ± 0.05	1.90 ± 0.03	0.30 ± 0.02	186	7.48

^a Hanner size distribution: $n(a) = (1 - a_0/a)^M (a_0/a)^N$; $a_0 = 0.1 \mu\text{m}$.

^b Peak grain size: $a_p = a_0(N + M)/N = 0.2 \mu\text{m}$ for every epoch.

^c Fractional filled volume of amorphous grains: $f = 1 - (a/a_0)^{D-3}$.

^d Number of peak grain size grains (i.e., scaling factor).

^e Number of free parameters.

TABLE 4
MASS RATIO TO TOTAL OF SUBMICRON-SIZED GRAINS

UT Dates (1)	Amorphous Pyroxene (2)	Amorphous Olivine (3)	Amorphous Carbon (4)	Crystalline Olivine (5)	Orthopyroxene (6)	Silicate/ Carbon (7)	Crystalline Silicate/ Amorphous Silicate (8)
1996 Oct 11–14.....	0.18	0.18	0.11	0.48	0.05	8.1	1.5
1997 Feb 14–15	0.20	0.10	0.07	0.58	0.05	13.3	2.1
1997 Apr 11.....	0.12	0.08	0.07	0.64	0.09	13.3	3.7
1997 Jun 24–25.....	0.21	0.09	0.10	0.52	0.08	9.0	2.0